



January 2018

Clustering Analysis Of Precipitation Sized Particles In Various Synoptic Regimes Using In Situ Observations

Samantha Carr

Follow this and additional works at: <https://commons.und.edu/theses>

Recommended Citation

Carr, Samantha, "Clustering Analysis Of Precipitation Sized Particles In Various Synoptic Regimes Using In Situ Observations" (2018). *Theses and Dissertations*. 2183.
<https://commons.und.edu/theses/2183>

This Thesis is brought to you for free and open access by the Theses, Dissertations, and Senior Projects at UND Scholarly Commons. It has been accepted for inclusion in Theses and Dissertations by an authorized administrator of UND Scholarly Commons. For more information, please contact zeinebyousif@library.und.edu.

CLUSTERING ANALYSIS OF PRECIPITATION SIZED PARTICLES IN VARIOUS
SYNOPTIC REGIMES USING IN SITU OBSERVATIONS

by

Samantha Susanne Carr
Bachelor of Science, University of North Carolina Asheville, 2016

A Thesis

Submitted to the Graduate Faculty

of the

University of North Dakota

in partial fulfillment of the requirements

for the degree of

Master of Science

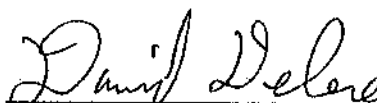
Grand Forks, North Dakota

August
2018

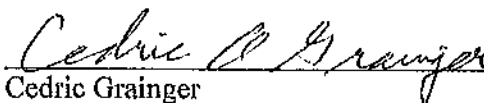
This thesis, submitted by Samantha Susanne Carr in partial fulfillment of the requirements for the Degree of Master of Science from the University of North Dakota, has been read by the Faculty Advisory Committee under whom the work has been done and is hereby approved.



Michael Poellot

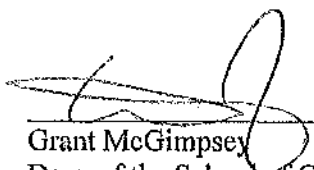


David Delene

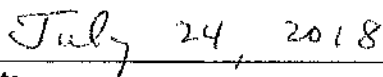


Cedric Grainger

This thesis is being submitted by the appointed advisory committee as having met all of the requirements of the School of Graduate Studies at the University of North Dakota and is hereby approved.



Grant McGimpsey
Dean of the School of Graduate Studies



Date

PERMISSION

Title Clustering Analysis of Precipitation Sized Particles in Various Synoptic Regimes using In Situ Observations

Department Atmospheric Sciences

Degree Master of Science

In presenting this thesis in partial fulfillment of the requirements for a graduate degree from the University of North Dakota, I agree that the library of this University shall make it freely available for inspection. I further agree that permission for extensive copying for scholarly purposes may be granted by the professor who supervised my thesis work or, in his absence, by the Chairperson of the department or the dean of the School of Graduate Studies. It is understood that any copying or publication or other use of this thesis or part thereof for financial gain shall not be allowed without my written permission. It is also understood that due recognition shall be given to me and to the University of North Dakota in any scholarly use which may be made of any material in my thesis.

Samantha Carr

June 14, 2018

TABLE OF CONTENTS

LIST OF FIGURES	vi
LIST OF TABLES	ix
ACKNOWLEDGMENTS	x
ABSTRACT	xii
CHAPTER	
I. INTRODUCTION	1
Motivation	1
Optical Array Probes	3
Poisson Process	5
Objectives	6
II. METHODOLOGY	8
Project Overview	8
Citation II Overview	9
Airborne Data Processing and Analysis Software Package	11
Software for OAP Data Analysis Version 2	12
Case Selection	13
Analysis	18
III. DATA	22
Data Overview	22
Prefrontal	22

Frontal	30
Postfrontal	34
I. RESULTS AND DISCUSSION	40
Overview	40
Prefrontal	40
Prefrontal Rain	41
Prefrontal Ice	47
Frontal	52
Postfrontal	57
Discussion	64
Synoptic Regimes	64
Spectral Density	66
II. CONCLUSIONS	68
Importance of Study	68
Conclusions	68
Implications and Future Work	69
REFERENCES	71

LIST OF FIGURES

Figure	Page
1. Example of a Poisson distribution where particles are uniformly, identically, and independently distributed random variables versus an example of a non-Poisson distribution where particles appear in a patchy or “clustered” manner	5
2. OLYMPEX observation network, from Houze et al. 2017	9
3. Configuration of the inboard vertically mounted HVPS-3 and outboard horizontally mounted HVPS-3	10
4. Idealization of the sectors of a typical extratropical cyclone passing over the OLYMPEX region, from Houze et al. 2017	14
5. 1500 UTC surface analysis for the 3 Dec 2015 (prefrontal) flight, obtained from the WPC and 15:25 UTC composite radar reflectivity obtained from the UCAR Image Archive using data from the College of DuPage’s NEXLAB	15
6. 2100 UTC surface analysis for the 23 Nov 2015 (frontal) flight, obtained from the WPC and 21:25 UTC composite radar reflectivity obtained from the UCAR Image Archive using data from the College of DuPage’s NEXLAB	16
7. 1800 UTC surface analysis for the 13 Dec 2015 (postfrontal) flight, obtained from the WPC and 17:25 UTC composite radar reflectivity obtained from the UCAR Image Archive using data from the College of DuPage’s NEXLAB	17
8. Randomly generated counts series. Pair correlation derived using the counts series. Spectral density of the randomly generated counts series.....	21
9. NPOL base reflectivity scan from 13 Nov 2015 at 15:37:27 UTC.....	24
10. NPOL base reflectivity scan from 13 Nov 2015 at 17:18:55 UTC.....	25
11. Sounding launched from the NPOL site on 13 Nov 2015 observed during 16:33 UTC	26

12. NPOL base reflectivity scan from 3 Dec 2015 at 15:37:29 UTC.....	27
13. NPOL base reflectivity scan from 3 Dec 2015 at 16:37:27 UTC.....	28
14. Sounding launched from the NPOL site on 3 Dec 2015 observed during 15:17 UTC	29
15. NPOL base reflectivity scan from 23 Nov 2015 at 21:37:30 UTC.....	31
16. NPOL base reflectivity scan from 23 Nov 2015 at 21:57:21 UTC.....	32
17. Sounding launched from the NPOL site on 23 Nov 2015 observed during 20:14 UTC	33
18. NPOL base reflectivity scan from 4 Dec 2015 at 14:57:19 UTC.....	35
19. Sounding launched from the NPOL site on 4 Dec 2015 observed during 15:18 UTC	36
20. NPOL base reflectivity scan from 13 Dec 2015 at 17:18:48 UTC.....	37
21. NPOL base reflectivity scan from 13 Dec 2015 at 18:18:49 UTC.....	38
22. Sounding launched from the NPOL site on 13 Dec 2015 observed during 15:17 UTC	39
23. Counts series for the 13 Nov 2015 flight during 16:28:30 UTC- 16:33:34 UTC. Pair correlation derived using the counts series. Spectral density of the derived spatial series during 16:28:30 UTC- 16:33:34 UTC	42
24. Counts series for the 13 Nov 2015 flight during 17:25:30 UTC- 17:31:10 UTC. Pair correlation derived using the counts series. Spectral density of the derived spatial series during 17:25:30 UTC- 17:31:10 UTC	43
25. Prefrontal rain flight leg parameter averages compared to the max pair correlation	46
26. Counts series for the 3 Dec 2015 flight during 15:36:40 UTC- 15:40:51 UTC. Pair correlation derived using the counts series. Spectral density of the derived spatial series during 15:36:40 UTC- 15:40:51 UTC	48

27. Counts series for the 3 Dec 2015 flight during 16:28:30 UTC- 16:32:22 UTC. Pair correlation derived using the counts series. Spectral density of the derived spatial series during 16:28:30 UTC- 16:32:22 UTC.....	49
28. Prefrontal ice flight leg parameter averages compared to the max pair correlation	51
29. Counts series for the 23 Nov 2015 flight during 21:26:40 UTC- 21:31:14 UTC. Pair correlation derived using the counts series. Spectral density of the derived spatial series during 21:26:40 UTC- 21:31:14 UTC	53
30. Counts series for the 23 Nov 2015 flight during 22:00:20 UTC- 22:05:50 UTC. Pair correlation derived using the counts series. Spectral density of the derived spatial series during 22:00:20 UTC- 22:05:50 UTC	54
31. Frontal flight leg parameter averages compared to the max pair correlation	56
32. Counts series for the 4 Dec 2015 flight during 14:54:34 UTC- 14:58:21 UTC. Pair correlation derived using the counts series. Spectral density of the derived spatial series during 14:54:34 UTC- 14:58:21 UTC	58
33. Counts series for the 13 Dec 2015 flight during 17:13:20 UTC- 17:17:31 UTC. Pair correlation derived using the counts series. Spectral density of the derived spatial series during 17:13:20 UTC- 17:17:31 UTC	60
34. Counts series for the 13 Dec 2015 flight during 18:18:20 UTC- 18:23:00 UTC. Pair correlation derived using the counts series. Spectral density of the derived spatial series during 18:18:20 UTC- 18:23:00 UTC	61
35. Postfrontal flight leg parameter averages compared to the max pair correlation	63
36. Max pair correlation of selected legs compared to the max spectral density	67

LIST OF TABLES

Table	Page
1. Prefrontal cases	23
2. Frontal cases	30
3. Postfrontal cases	34
4. Prefrontal rain flight leg averages (excluding max pair correlation)	45
5. Prefrontal ice flight leg averages (excluding max pair correlation)	50
6. Frontal flight leg averages (excluding max pair correlation)	55
7. Postfrontal flight leg averages (excluding max pair correlation)	62
8. Correlation coefficient, r , from each sector in regards to derived parameters and parameters observed in-situ	64
9. Max pair correlation and max spectral density observed for selected flight legs	67

ACKNOWLEDGMENTS

I would like to express my sincere appreciation to my advisor, Professor Michael Poellot, for his guidance during my time here at the University of North Dakota. Thanks to his encouragement, I have not only accomplished another milestone, but have also become more confident that I do belong in this field. I would also like to thank my other committee members, Drs. David Delene and Cedric Grainger, for their guidance and feedback during this process.

To Dr. Christopher Godfrey, my undergraduate advisor, I would not be here today without your patience, guidance, and honesty. You not only inspired me, but also saw something in me that I didn't see in myself. For that, I can never thank you enough. I can only hope that I have an impact on someone's life like you had on mine.

To my parents, there are not enough words to describe how thankful I am to the both of you. I'd be nowhere near the person I am and the person I'm still working on becoming, without your unconditional love and constant support. Thank you for believing in this dream that I have been chasing since 2nd grade, and believing in me when I didn't believe in myself.

To Joe, my lovely officemate, thank you for all of your guidance and friendship. Because of you, I have a solid foundation for coding, even though there were many tears along the way. To Alex, my closest friend, I will be forever thankful for your companionship during our graduate career. You have left a tremendous impact on my life and continue to inspire me. Thank you for accepting me, loving me, and supporting me

through thick and thin. I am incredibly fortunate to have someone like you in my life and wouldn't have survived graduate school without you.

Lastly, I would like to thank my cat, Simba. Adopting you was the single greatest choice I have ever made. Thanks for being excited to see me when I get home, for all the snuggles when I get lonely, and for making me laugh so hard that my stomach hurts. You have been by my side throughout my whole graduate career and honestly deserve an honorary M. S degree.

ABSTRACT

It is widely assumed that cloud particles are spatially distributed in a random and uncorrelated fashion (a Poissonian distribution); however, previous studies using airborne observations have shown this is not true for small cloud droplets. Previous work using rain gauges and disdrometer networks have also found this to be true for precipitation size particles; however, little research has been done using airborne observations to study such phenomena. Thus, a question to be addressed in this study is whether clustering of precipitation size particles can be examined using airborne observations.

In situ microphysical data collected on the University of North Dakota Citation II research aircraft during the Olympic Mountains Experiment (OLYMPEX) using a Stratton Park Engineering Company (SPEC) High Volume Precipitation Spectrometer Version 3 (HVPS-3) are analyzed. The HVPS-3 captures shadow images of precipitation size particles, which can be used to examine clustering signatures on meter to kilometer size scales. Flight data are also stratified by the synoptic classifications used in OLYMPEX to determine if clustering changes with synoptic forcing. Overall, preliminary results indicate that clustering can be examined using airborne observations and that differences do occur between synoptic regimes. Results from this study also emphasize that non-Poisson statistics should be incorporated into the current radar framework, as a considerable amount of research has indicated that particles are not uniformly distributed in space.

CHAPTER 1

INTRODUCTION

Motivation

When viewed from space, the visual appearance of Earth is dominated by clouds and their patterns. Clouds exist because of the physical process of condensation, and condensation occurs mainly in response to dynamical processes that include widespread vertical air motions, convection, and mixing (Rogers and Yau 1989). Accordingly, the pattern and structure of clouds are influenced by dynamical factors such as stability, convergence, and the proximity of fronts and cyclones (Rogers and Yau 1989). In regards to precipitation, initiation can occur via collision-coalescence or as a result of the Wegener-Bergeron-Findeisen process, which involves the growth of ice particles at the expense of liquid droplets in mixed-phase clouds (i.e. consisting of both liquid droplets and ice particles) (Storelvmo and Tan 2015). While particle formation and growth are of fundamental importance to cloud physics, an understanding of the spatial distribution, or “clustering”, of clouds and precipitation particles is also of equal importance. Previous studies on the clustering of cloud particles have emphasized that the drop size distribution can broaden rapidly due to enhanced collision and condensation rates. Additionally, these studies have provided insight on why remotely sensed cloud drop size is generally larger than that measured in situ (Marshak et al. 2005). However, those studies only examined clustering of cloud particles on small spatial scales (centimeter to meter), in order to avoid

assumptions that would become unavoidable when using larger spatial scales (i.e. clouds being uniform).

Despite the more recent advances in instrumentation, the degree of clustering of precipitation size particles still remains unknown. The clustering of precipitation size particles can have implications for Rayleigh statistics, as it would violate the assumption that conditions are spatially homogeneous (Jameson and Kostinski 2008). Thus, knowledge concerning the spatial distribution of precipitation particles and clustering at larger spatial scales is needed. Additionally, using Monte Carlo experiments, Jameson and Kostinski 2008 found that clustering of particles increases the standard deviation of the differential reflectivity (Z_{DR}) beyond what is usually calculated assuming Rayleigh (randomly distributed particles) statistics. As a result, findings from this study could shed light on whether non-Rayleigh signal statistics should be used in radar applications.

While the measurement of precipitation at a given location using surface-based instruments is relatively straightforward, the large spatial and temporal variability of precipitation intensity, type, and occurrence make direct measurements difficult over large regions, especially over the oceans (Hou et al. 2014). For example, rain gauges suffer from representativeness issues when estimating precipitation over extended areas, and radars, where available, must contend with issues such as attenuation, unknown particle composition and size distributions, and beam blockage in mountainous regions (Hou et al. 2014). To compensate for these issues, space-based remote sensing instrumentation is often used. The Global Precipitation Measurement (GPM) satellite was launched in February 2014 by the U.S National Aeronautics and Space Administration (NASA) and the Japan Aerospace Exploration Agency (JAXA) to help accurately measure global rain and

snowfall amounts. With its onboard Dual-Frequency Precipitation Radar (DPR) and 13-channel GPM Microwave Imager (GMI), the GPM satellite expands and extends into future decades the nearly global surveillance of precipitation previously provided by the Tropical Rainfall Measuring Mission (TRMM) satellite and broadens coverage to higher latitudes (Houze et al. 2017). Importantly, the DPR and GMI measurements are used to estimate precipitation rates through the use of retrieval algorithms. These algorithms must be refined and validated through the use of coincident in situ observations of the microphysical properties of precipitation particles (Hou et al. 2014).

Optical Array Probes

Our present state of knowledge of the microstructure of clouds and precipitation can be traced primarily to the ability to obtain information about particles from samples collected from aircraft (Knollenberg 1970). Direct sampling techniques were used initially, but measurement accuracy was adversely affected by a number of problems including low sampling rate, discontinuous sampling, and disturbing the sample. Thus, indirect sampling techniques were developed. Because of advances in optics and photo-electrics, brought about primarily by the birth of the laser industry, an optical approach was developed (Knollenberg 1970). Currently a variety of optical array probes (OAPs) are used to measure the concentration and size distribution of cloud particles. OAPs measure the sizes of shadows produced by particles passing through a collimated, high intensity, monochromatic light beam that illuminates a linear array of diodes (Knollenberg 1970). When a particle passes through the light beam within the sampling area, the diode elements that have the light reduced by 50 % or less are set to 1, while diodes with greater than

50 % light are set to 0. Hence, the photodiode is considered to be occulted if the intensity of the background illumination is attenuated by more than 50 % (Korolev and Issac 2005).

One advantage of OAPs, and imaging systems in general, is that the depth of field increases with the square of the particle size, thus, the sampling volume always increases with increasing particle size, partially compensating for the decrease in concentration (Knollenberg 1970). However, inherent in the design of the older imaging probes were counting and sizing errors due to the relatively slow response time, which prompted order-of-magnitude errors in determining the particle size distribution (PSD) of particles less than 100 microns (Lawson et al 2006). The latest generation of OAPs have significantly improved response times and higher resolutions. The current study uses measurements made with a High Volume Precipitation Spectrometer Version 3 optical array probe (HVPS-3 OAP). The HVPS-3(s) optics are configured for 150 μm resolution, which allows particles up to 1.92 cm in diameter to be completely imaged.

Another inherent problem associated with OAPs, and airborne instruments in general, is particle shattering caused by collision with the probe or the aircraft. The probability of shattering depends upon the ice particle habit, size, probe housing, and airspeed and it can affect the calculations of the concentration, water content, and radar reflectivity derived from the probe measurements (Korolev and Issac 2005). To minimize the effects of particle shattering, modified tips and post-processing rejection of particles via interarrival time are used. However, the rejection of particles based on interarrival times is not entirely satisfactory, especially since the correction methodology is based upon the assumption that the particles are randomly distributed, which, although satisfactory as a first approximation, may not be entirely appropriate (Field et al. 2006).

Poisson Process

The assumption of statistically uniform and independently distributed positions of droplets in homogeneous unmixed clouds underlies much of cloud physics (Roger and Yau 1989). For example, the stochastic collection equation which describes the growth of droplets via collision and coalescence, assumes that the cloud particles are spatially distributed in a perfect random fashion, that is, according to the Poisson process (Kostinski and Shaw 2001). Visually, Poissonian distributions appear devoid of structure and resemble an ideal gas of molecules, whereas non-Poissonian distributions appear patchy or “clustered” (Shaw et al. 2002, Fig. 1). More precisely, the assumptions behind the Poisson process are: (i) the process is statistically homogeneous; (ii) the probability of detecting more than one particle in a given volume dV is vanishingly small for sufficiently small dV ; (iii) particle counts in non-overlapping volumes are statistically independent random variables at any length scale (Kostinski and Shaw 2001).

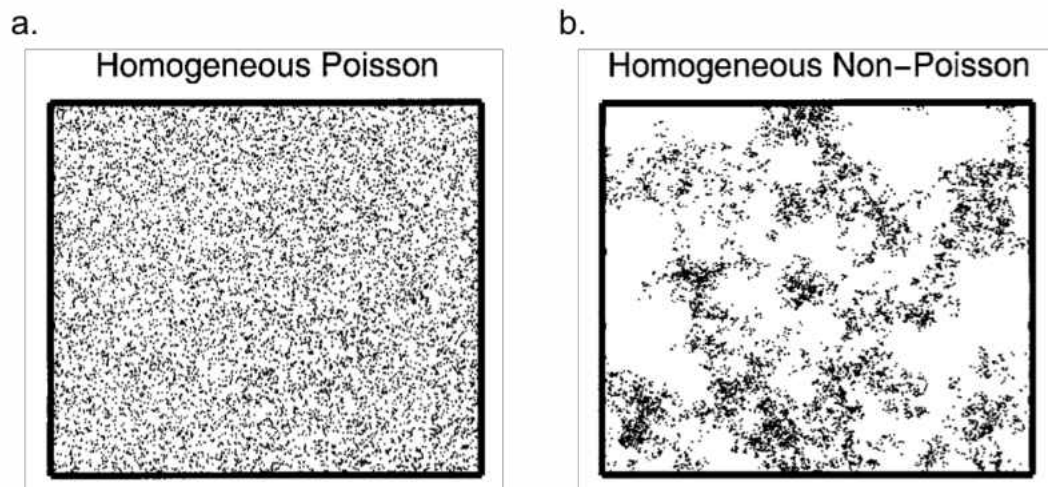


Figure 1: Example of a Poisson distribution (a), where particles are uniformly, identically, and independently distributed random variables versus an example of a non-Poisson distribution (b), where particles appear in a patchy or “clustered” manner. Figure reproduced from Shaw et al. 2002.

Previous studies, however, have provided results that conflict with the current Poissonian assumption. In an analysis of Forward Scattering Spectrometer Probe (FSSP) measurements of cloud droplet distributions, Baker (1992) reported non-Poissonian deviations in convective cumulus clouds down to scales of several centimeters, an effect he attributed to small-scale turbulence. Similarly, using a pair-correlation function, which measures the departure from a Poisson process, Shaw et al. (2002) found a clear enhancement of droplet clustering. In regards to precipitation size particles, using a network of 19 optical disdrometers in Charleston, South Carolina. Jameson et al. (2015) found that both spatial and temporal clustering play a role in rain variability depending upon the drop size. Additionally, their work determined that differences in spatial and temporal clustering do occur in different types of precipitation (convective and stratiform). Along with the use of disdrometers, the clustering of rain can also be found up to at least the typical kilometer scales of most radar volumes. However, little work has examined the clustering of precipitation size particles using airborne observations.

Objectives

The objective of this work is to study the clustering of precipitation size particles using in situ airborne observations. Information on the spatial distribution may provide insight on the evolution of precipitation and may also shed light on physical mechanisms acting on the precipitation process (Kostinski and Jameson 1997). Though previous studies cited above found evidence of cloud size particle clustering on centimeter to meter scales, the use of the HVPS-3 in this study allows clustering to be examined on meter to kilometer size scales. Data collected from the Olympic Mountains Experiment (OLYMPEX) are stratified by the synoptic classifications used in OLYMPEX (pre-frontal, warm sector,

frontal, and post-frontal) to determine if clustering changes with synoptic forcing. Additionally, analysis of the HVPS-3 data attempts to assess and provide any additional impacts in regards to the atmospheric science and remote sensing communities.

CHAPTER 2

METHODOLOGY

Project Overview

This study is based on data gathered during the NASA Olympic Mountains Experiment (OLYMPEX), which was conducted as part of NASA's GPM satellite Ground Validation Program. OLYMPEX was an international, multi-organization field campaign designed to collect detailed measurements by aircraft and ground sites to correspond with GPM satellite measurements (Houze et al. 2017). The project took place between November 2015 and February 2016 in Washington State, and aimed to validate assumptions used in precipitation measurement algorithms. The venue for OLYMPEX, as seen in Fig. 2, was chosen because it has precipitation from midlatitude baroclinic storm systems arriving frequently from the adjacent Pacific Ocean and abruptly transiting mountainous terrain (Houze et al. 2017). In addition, several airfields capable of serving large aircraft exist in the region, and the area of the Olympic Mountains is small enough that the OLYMPEX aircraft could fly in and over the incoming storms for long periods of time with minimal time spend traversing the distance to and from the observation area (Houze et al. 2017).

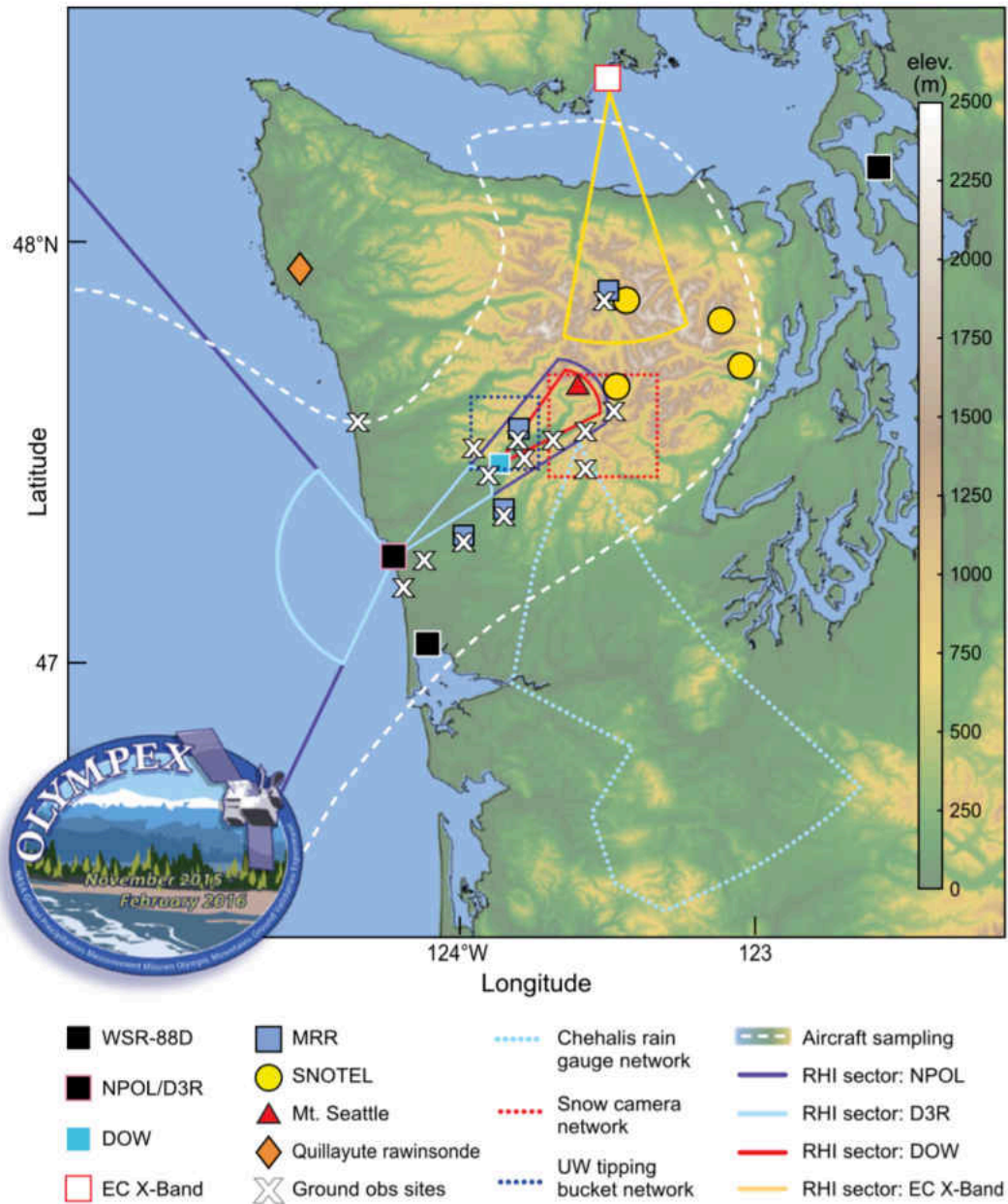


Figure 2: The Olympic Mountains Experiment (OLYMPEX) observation network, from Houze et al. 2017.

Citation II Overview

The platform used to obtain in-situ cloud measurements during OLYMPEX was the University of North Dakota Citation II research aircraft (UND Citation II). This aircraft was modified for atmospheric research and was capable of providing in-situ aerosol and

cloud microphysical measurements at altitudes from near the surface to 13 km (O'Brien 2016). Structural modifications to the UND Citation II included pylons beneath the wing tips to allow for mounted instruments, hard points on the fuselage to hold instruments that exceeded the size and weight limits of other areas, and a nose boom which collected pressure and wind measurements ahead of the aircraft nose. While the UND Citation II featured a variety of different instruments, this study solely focuses on the HVPS-3. During OLYMPEX there were two HVPS-3 OAPs mounted underneath the left wing, as seen in Fig. 3. The HVPS-3 on the inboard pylon was always mounted vertically, whereas the orientation of HVPS-3 on the outboard pylon was modified depending on the day. However, the outboard HVPS-3 was generally mounted horizontally in order to obtain measurements in an orthogonal direction from the inboard HVPS-3.



Figure 3: The configuration of the inboard vertically mounted High Volume Precipitation Spectrometer Version 3 (HVPS-3) (left) and outboard horizontally mounted HVPS-3 (right). The orientation of the outboard HVPS-3 was modified depending on the day.

No matter the configuration, the UND Citation II data system always recorded basic parameters such as position, altitude, and speed. Additionally, the meteorological package included measurements of temperature, dew point temperature, pressure, and three-dimensional winds. The Science Engineering Associates (SEA) Model M300 Data Acquisition System, also onboard the UND Citation II, is customized for each project in order to accommodate specific research demands. The M300 not only records and displays data in real time, but also calculates physical parameters such as the true airspeed (i.e. airspeed corrected for temperature and altitude). True airspeed (TAS) is a critical parameter for OAP measurements, since the sample volume is dictated by the TAS of the aircraft and affects particle images, sizing, and concentrations (O'Brien 2016). All instrument data acquired by the M-300 are saved in a binary formatted file (*.sea), and data from each of the SPEC instruments (2DS, HVPS3, Cloud Particle Imager) are recorded by a different Windows XP computer in a binary formatted file (O'Brien 2016).

Airborne Data Processing and Analysis Software Package

The development of software to effectively process and analyze measurements is a crucial aspect of any research project. To quality control and assure data collected with the UND Citation II, the Airborne Data Processing and Analysis (ADPAA) package was developed. The ADPAA package is intended to fully automate data processing while incorporating the concept of missing value codes and levels of data processing (Delene 2011). ADPAA processing is split into four different processing levels. The first level splits the saved binary data from the M-300 into files for each instrument system. The second level converts parameters from engineering units (e.g. volts) to physical units (e.g. Celsius) (Delene 2011). The third level combines parameters from multiple instruments to derive

other parameters, such as liquid water content and ambient temperature. Lastly, the fourth level combines derived parameters from Level 3 data files to create combined files, such as combining spectra from the Cloud Droplet Probe (CDP), 2D-S, and HVPS-3. The final step in the data processing is to create a summary file that contains all parameters of scientific interest (Delene 2011). As a result, the summary file can contain parameters from any level. Additionally, each flight is then analyzed to quality assure the data, which entails removing any invalid data and applying a parameter specific missing value code for that time frame.

The data obtained during OLYMPEX using the UND Citation II were processed using the ADPAA software on 26 April 2016. Of particular interest is the temperature, pressure altitude, and GPS position, since these measurements define the sampling environment of the HVPS3 probe. Additionally, the TAS is important since it is used to convert from a time series to a spatial series. However, a quality-assured TAS is needed for the post-processing of OAP data because the TAS sent to the SPEC probes during flight is not recorded by OAPs.

Software for OAP Data Analysis Version 2

The data collected with the HVPS-3(s) during OLYMPEX were processed with Software for OAP Data Analysis Version 2 (SODA2), which was developed by Aaron Bansemer at the National Center for Atmospheric Research (NCAR). The SPEC data acquisition software stores photodiode array data within binary files. While there were two HVPS-3(s) flown in OLYMPEX, only data collected from the outboard mounted HVPS-3 are analyzed. In order to size each particle image within a data buffer, SODA2 uses the

‘circle fit method’, which encloses each image with the smallest possible circle. The diameter of the particle is defined as the diameter of the bounding circle. Additionally, SODA2 allows for the creation of particle by particle (pbp) files, which stores information about each individual particle, including particle diameter and inter-particle time (IPT, i.e. time between the current particle and the previous particle). For analysis purposes, the pbp data are converted from an Interface Definition Language (IDL) save file format into an American Standard Code for Information Interchange (ASCII) file, in the standard NASA/UND format (Delene 2009). Lastly, the quality assured TAS located in the .basic file is merged into the converted pbp file.

Case Selection

OLYMPEX benefited from cooperative weather that provided large amounts of precipitation from a series of synoptically well-defined storms (Houze et al. 2017). The Pacific frontal systems passing over the Olympic Peninsula typically have four sectors, each with different environmental characteristics, cloud patterns, and precipitation characteristics (Houze et al. 2015). Fig. 4 shows an idealized storm structure consisting of the four sectors (i.e. prefrontal, frontal, postfrontal, and warm), which was used to guide daily forecast and planning of OLYMPEX operations.

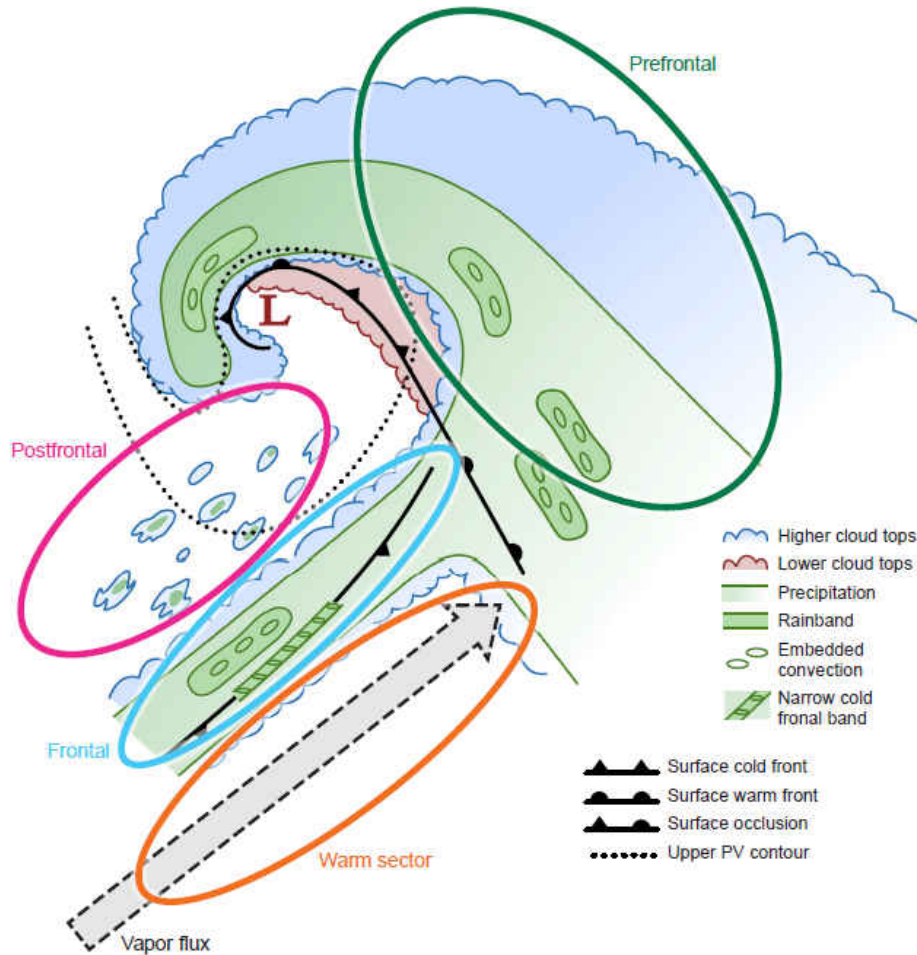


Figure 4: Idealization of the sectors of a typical extratropical cyclone passing over the Olympic Mountains Experiment (OLYMPEX) region, from Houze et al. 2017.

The prefrontal sector is generally located to the east and north of an occluded front and north of a warm front (if present), and is generally characterized by warm advection and broad stratiform clouds with steady rainfall (Houze et al. 2015). However, rain rates can vary depending on the moisture content and degree of synoptic and mesoscale forcing. An example surface analysis and composite radar reflectivity image observed during an OLYMPEX prefrontal flight (3 Dec 2015) can be seen in Fig. 5. Though the surface analysis does not completely agree with what was previously described, it is important to note that Fig. 4 is an idealization.

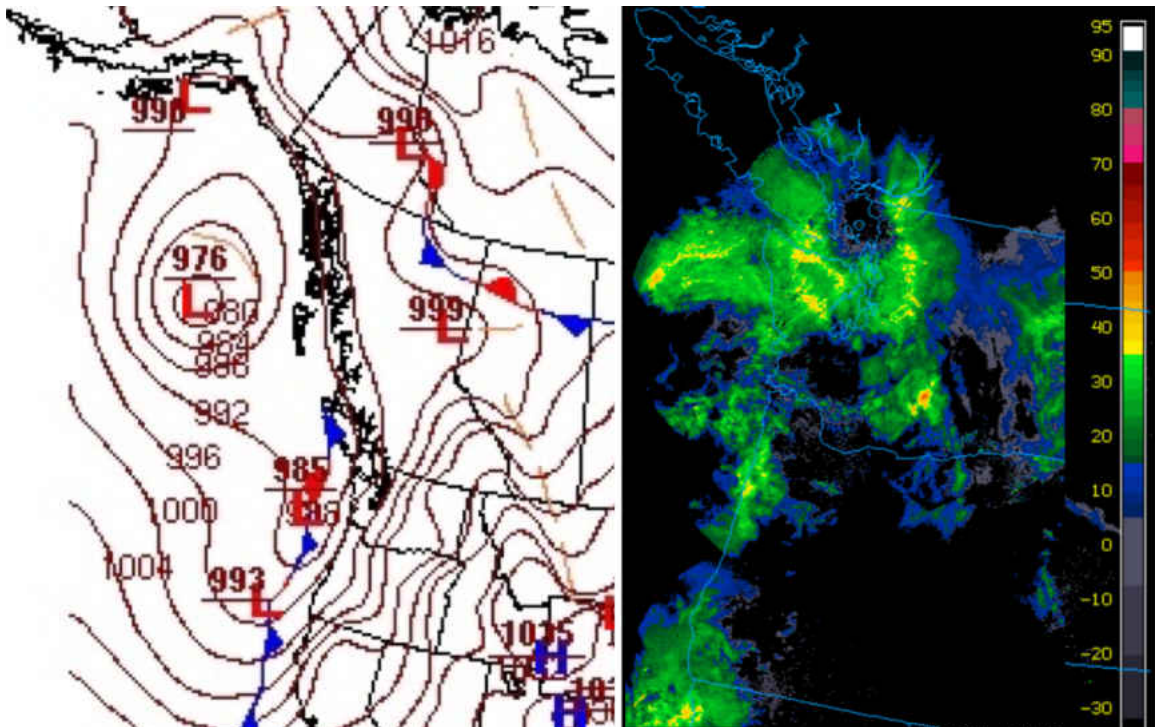


Figure 5: 1500 UTC surface analysis (left image) for the 3 Dec 2015 (prefrontal) flight, obtained from the Weather Prediction Center (WPC). 15:25 UTC composite radar reflectivity (right image) for the 3 Dec 2015 (prefrontal) flight, obtained from the University Corporation for Atmospheric Research (UCAR) Image Archive using data from the College of DuPage's NeXt Generation Weather Lab (NEXLAB).

The frontal sector is a broad quasi-linear cloud shield within a cold (or occluded) front and its associated frontal circulations contribute to the production of precipitation (Houze et al. 2015). The frontal sector is often associated with a wide cold-frontal rain band, which additionally has a narrow cold-frontal rain band embedded within it that produces high rainfall rates. An example surface analysis and composite radar reflectivity image observed during an OLYMPEX frontal flight (23 Nov 2015) can be seen in Fig. 6. Though rainbands in these sectors can produce substantial rainfall amounts, only a few millimeters of rain fell during this stratiform event.

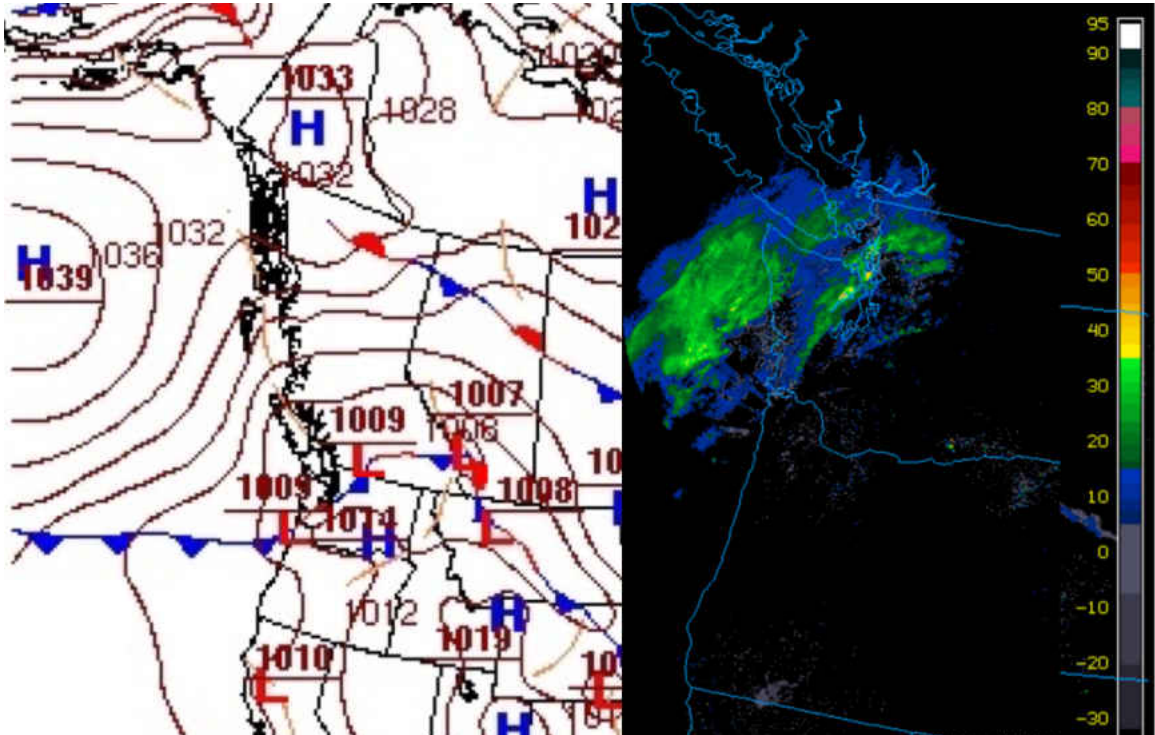


Figure 6: 2100 UTC surface analysis (left image) for the 23 Nov 2015 (frontal) flight, obtained from the Weather Prediction Center (WPC). 21:25 UTC composite radar reflectivity (right image) for the 23 Nov 2015 (frontal) flight, obtained from the University Corporation for Atmospheric Research (UCAR) Image Archive using data from the College of DuPage’s NeXt Generation Weather Lab (NEXLAB).

The postfrontal sector is situated behind (west) of the cold (or occluded) front and is characterized by cold advection, conditional instability and a field of small-scale convective clouds separated by clean air (Houze et al. 2015). As a result, precipitation in the postfrontal sector can significantly contribute to the total rain or snowfall produced by the entire storm system. An example surface analysis and composite radar reflectivity image observed during an OLYMPEX postfrontal flight (13 Dec 2015) can be seen in Fig. 7. The surface analysis is nearly identical to the idealization provided in Fig. 4, and convection is present along the coast of Washington as indicated by the high reflectivity values (~ 50 dBZ). Lastly, warm sector rainbands, which resemble squall lines, are oriented parallel to the approaching cold front (Matejka et al. 1979).

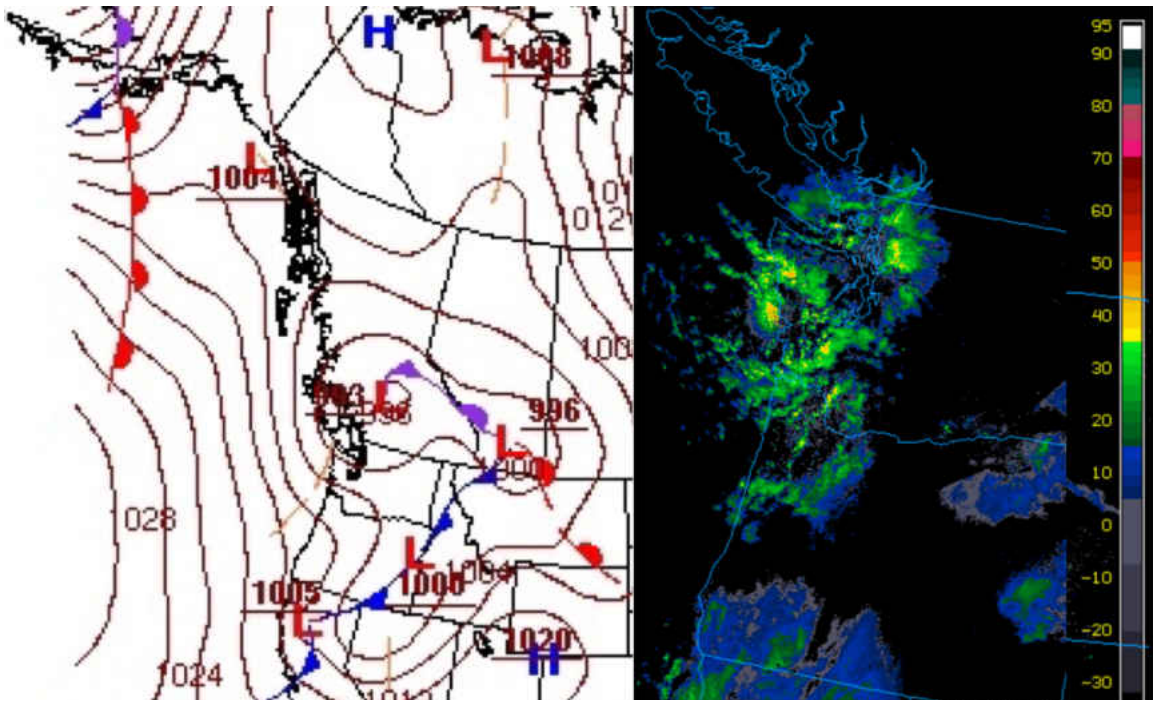


Figure 7: 1800 UTC surface analysis (left image) for the 13 Dec 2015 (postfrontal) flight, obtained from the Weather Prediction Center (WPC). 17:25 UTC composite radar reflectivity (right image) for the 13 Dec 2015 (postfrontal) flight, obtained from the University Corporation for Atmospheric Research (UCAR) Image Archive using data from the College of DuPage's NeXt Generation Weather Lab (NEXLAB).

Throughout the course of OLYMPEX, the UND Citation II sampled eight prefrontal, eight warm, two frontal and six postfrontal sectors. In order to determine if clustering changes with synoptic forcing, flights from each sector are analyzed. Since the warm sector was usually sampled during prefrontal flights, this study chose to solely focus on prefrontal, frontal and postfrontal sectors. Cases are determined through extensive search of science notes taken by instrument operators during each flight, as they provide additional information on the sampled atmospheric environment. Additionally, since it is desirable to use data at a constant altitude, pressure altitude data for each flight are inspected. Lastly, since the outboard HVPS-3 was mounted horizontally for every flight except two, no cases in this analysis occur on days when the HVPS-3 was mounted

vertically, in an effort to provide uniformity.

Analysis

While viewing shadow images produced by the HVPS3 can be used for qualitative purposes, a quantitative approach is needed to determine whether clustering exists. Since the HVPS-3 records particle data in terms of time, the data are first converted into a spatial series and then summed to create a cumulative particle distance series (CPD), as seen in Equation 1, which ultimately represents how far the plane has traveled.

$$CPD_i = \sum_{n=1}^i IPT_n * TAS_n, \quad (1)$$

Using data from the pbp file and the derived cumulative spatial series, a counts series is computed by determining how many particle counts exist within each ten meters. To qualify as a count, the IPT must be greater than 0.0001 seconds, which prevents any shattered particles from being accepted. Additionally, in an effort to reduce noise, the first three channels of the HVPS-3 were excluded. Thus, each particle is comprised of at least three pixels (450 μ m). Additionally, to keep things uniform among each flight and sector, only those spatial series that are 30 kilometers in length and at a constant pressure altitude are used.

To quantify clustering, the pair correlation function is used and is calculated by

$$\eta(r) = \left(\frac{1}{N^2} \right) \overline{N(r_o)N(r_o + r)} - 1, \quad (2)$$

where N is the number of droplets in volume V, and r is an independent variable (length-scale, i.e. lag). The pair correlation quantifies clustering by comparing measured spatial distributions with a standard of perfect randomness and it does so in a scale-localized

manner (Shaw et al. 2002). The pair correlation function is zero if a Poisson process is observed. However, when the pair correlation is greater than zero it implies that if a particle is encountered at a given position in a cloud, there is an enhanced probability of finding another particle distance r away (Shaw et al. 2002). For this analysis, the maximum r (i.e. lag) is one tenth of the total flight leg distance (i.e. a 30 km flight leg would result in a maximum r of 3 km).

To determine if any correlations between particle size and clustering exist, the mean diameter, which is defined as the average particle diameter within the particle size spectrum, is calculated by

$$\text{Mean Diameter} = \frac{D_{10}}{N_{10}} \quad (3)$$

where D_{10} is the sum of the total particle diameters per 10 meters and N_{10} is the total number of particle counts per 10 meters. Additionally, the mean volume diameter, which is defined as the mean diameter of the volume distribution, is calculated by

$$\text{Mean Volume Diameter} = \left(\frac{6}{\pi}\right) (\bar{V}_{10})^{1/3} \quad (4)$$

where \bar{V}_{10} is the average volume per 10 meters, which is computed by dividing the total volume in each 10 meters by the total number of counts in each 10 meters. The mean volume diameter is useful as it provides a size-weighted average that can be related to radar reflectivity, and can help determine whether clustering is observed more frequently for larger size particles.

This study also examines the spectral density of each flight leg's spatial series to determine how the spectral density is distributed across multiple frequencies. Lower frequencies represent larger distances (i.e. a frequency of 0.010, 0.100, and 1.000

represents a length scale of 10 km, 1 km, and 100 m respectively), assuming a TAS of 100 m s⁻¹. These minima and/or maxima of spectral density are then compared to the pair correlation to determine if any patterns exist. For example, enhanced variance at small scales may be related to a peak in the pair correlation function observed at similar scales (Shaw et al. 2002). The spectral density is plotted using Cplot, a software program developed by David Delene, and calculated by

$$P(k) = \frac{1}{2\pi} \int_{-\infty}^{\infty} \rho(r) e^{-ikr} dr, \quad (5)$$

which takes the auto-covariance of the individual spatial series created earlier. Lastly, the pair correlation for each flight leg is compared to the average number of counts, pressure altitude, temperature, and turbulence of each flight leg to determine if any additional correlations exist.

To test the computational methods, the pair correlation function and spectral density were calculated for a randomly generated series of counts (Fig. 8). As expected, the pair correlation at each lag is zero and the spectral density is flat, indicating that a Poissonian distribution is observed.

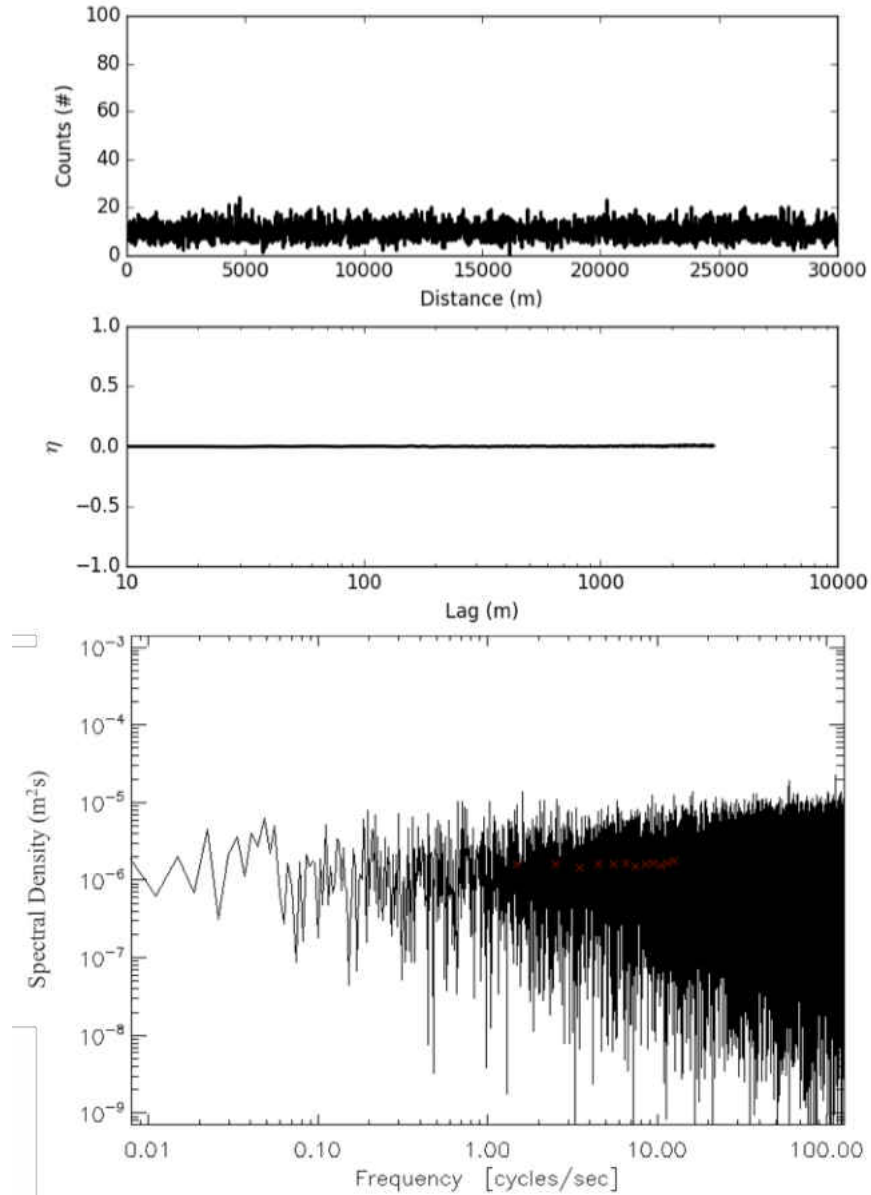


Figure 8: Randomly generated counts series (top image). Data represents the number of counts observed per 10 meters. Pair correlation (middle image) derived using the counts series above. Maximum lag is one-tenth of the total distance. Spectral density (bottom image) of the randomly generated counts series.

CHAPTER III

DATA

Data Overview

This chapter presents select cases from each sector and the total number of cases that are used within the analysis. Case study days for each frontal sector are selected through review of daily science summaries from OLYMPEX along with inspection of the UND Citation II pressure altitude data. The Citation data are then broken down into shorter flight segments or legs. In this analysis, each flight leg consists of a constant pressure altitude, is 30 km in length, and has an average time of four to five minutes. For each case, a NASA dual-polarization S-band radar (NPOL) base reflectivity image and an atmospheric sounding are shown to provide background on the sampled environment. Additionally, the flight leg track is superimposed on the NPOL base reflectivity image to provide a visual reference of the location of the Citation in relation to the overall precipitation field and geographical references.

Prefrontal

A total of thirteen prefrontal flight legs are used in this analysis (Table 1). From those thirteen flight legs, four representative cases are selected, as highlighted in Table 1.

Table 1: Prefrontal cases. Highlighted times indicate flight legs chosen for thorough analysis.

Date	Start Time	End Time	Average Pressure Altitude
13 Nov 2015	15:15:50 UTC	15:19:33 UTC	3100 m
	16:11:40 UTC	16:50:55 UTC	3099 m
	16:28:30 UTC	16:33:34 UTC	1572 m
	16:56:40 UTC	17:01:55 UTC	1570 m
	17:25:30 UTC	17:31:10 UTC	655 m
	17:35:30 UTC	17:40:47 UTC	1556 m
	18:10:00 UTC	18:14:44 UTC	1265 m
3 Dec 2015	14:38:20 UTC	14:41:52 UTC	5676 m
	15:03:20 UTC	15:07:18 UTC	4300 m
	15:36:40 UTC	15:40:51 UTC	3224 m
	16:17:10 UTC	16:21:22 UTC	4446 m
	16:28:30 UTC	16:32:22 UTC	5813 m
	16:40:00 UTC	16:44:01 UTC	4144 m

The first and second cases occurred on 13 November 2015. Fig. 9 (Fig. 10) shows the closest NPOL base reflectivity scan in relation to the first case (second case). Though the first case occurred more than 51 minutes after the closest base reflectivity scan, the overall structure of precipitation remained the same during the flight leg. Thus, the first case occurred in regions of reflectivity primarily between 15-25 dBZ. Similarly, the second case occurred in regions of reflectivity primarily between 25-30 dBZ. The sounding launched from the NPOL site during the first case and prior to the second case shows saturated conditions from the surface to nearly 650 hPa, followed by a dry layer near the cloud top, which then transitions to a relatively moist layer near the top of the troposphere

(Fig. 11). The sounding also shows weak southwesterly winds near the surface with stronger westerly winds aloft.

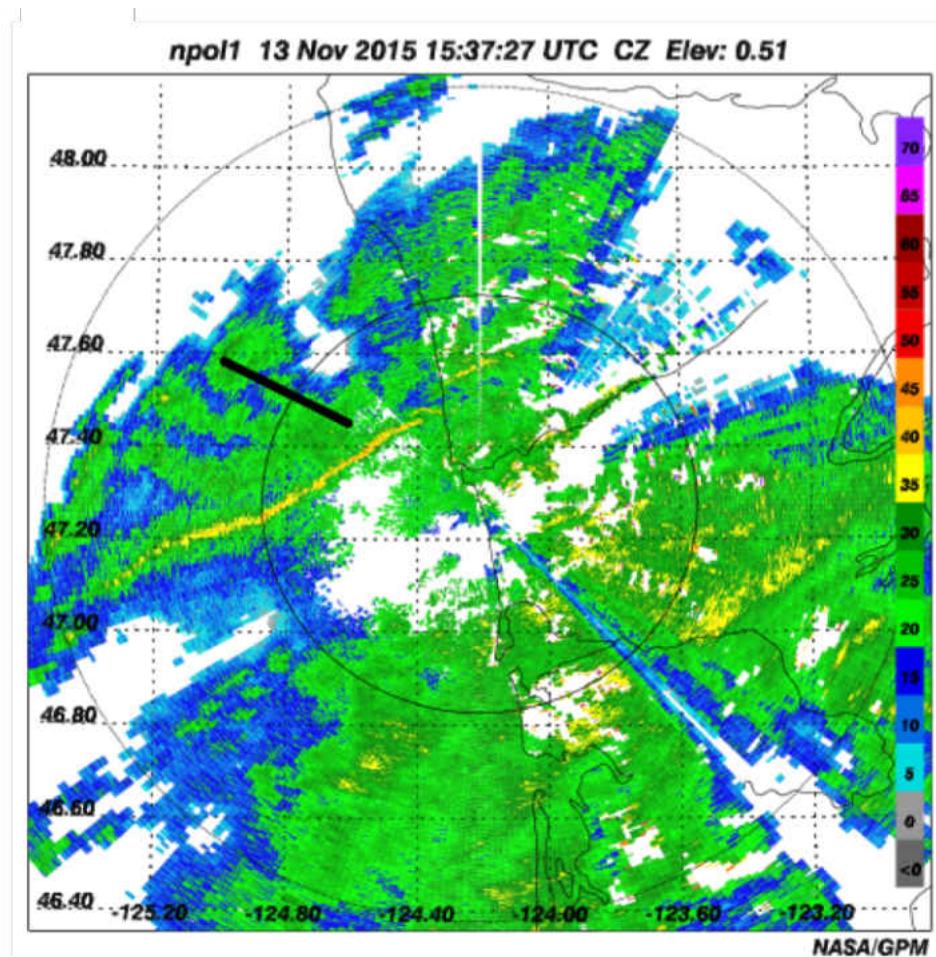


Figure 9: NASA dual-polarization S-band radar (NPOL) base reflectivity scan from 13 Nov 2015 at 15:37:27 UTC (leg start time -51:03). The black line indicates the position of the UND Citation II during 16:28:30 UTC – 16:33:34 UTC.

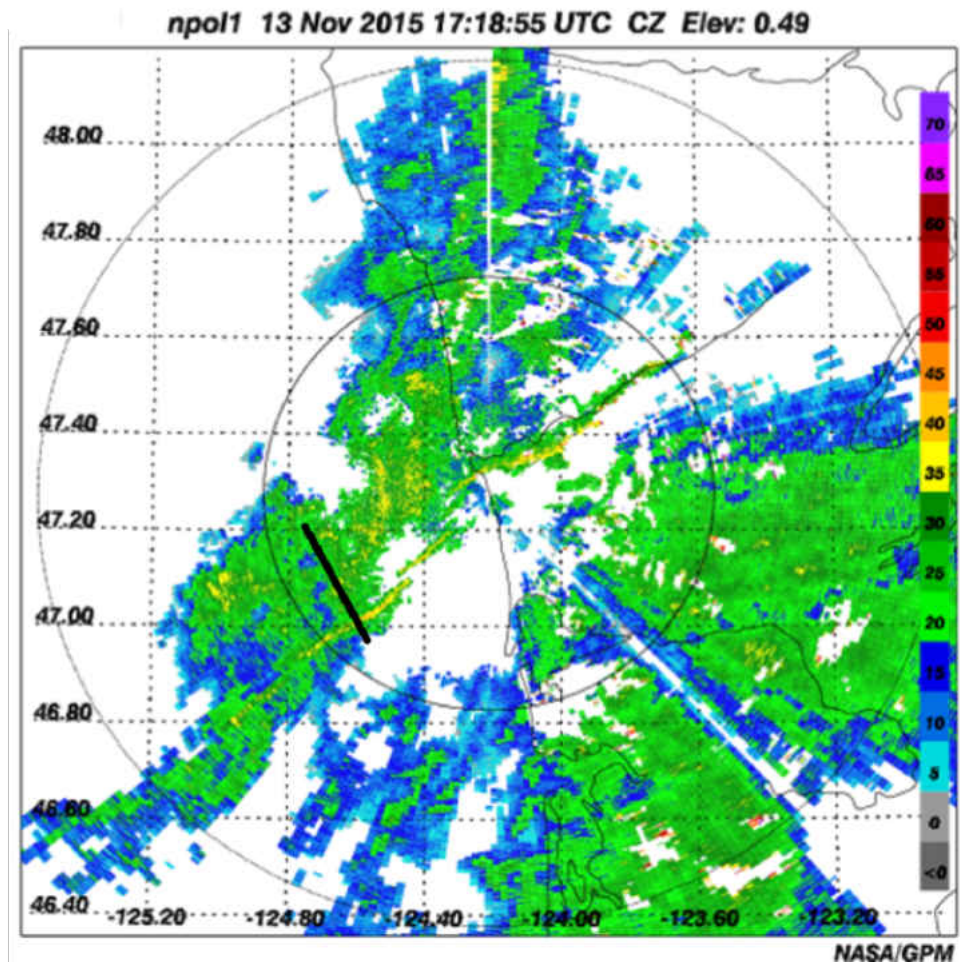


Figure 10: NASA dual-polarization S-band radar (NPOL) base reflectivity scan from 13 Nov 2015 at 17:18:55 UTC (leg start time –6:35). The black line indicates the position of the UND Citation II during 17:25:30 UTC – 17:31:10 UTC.

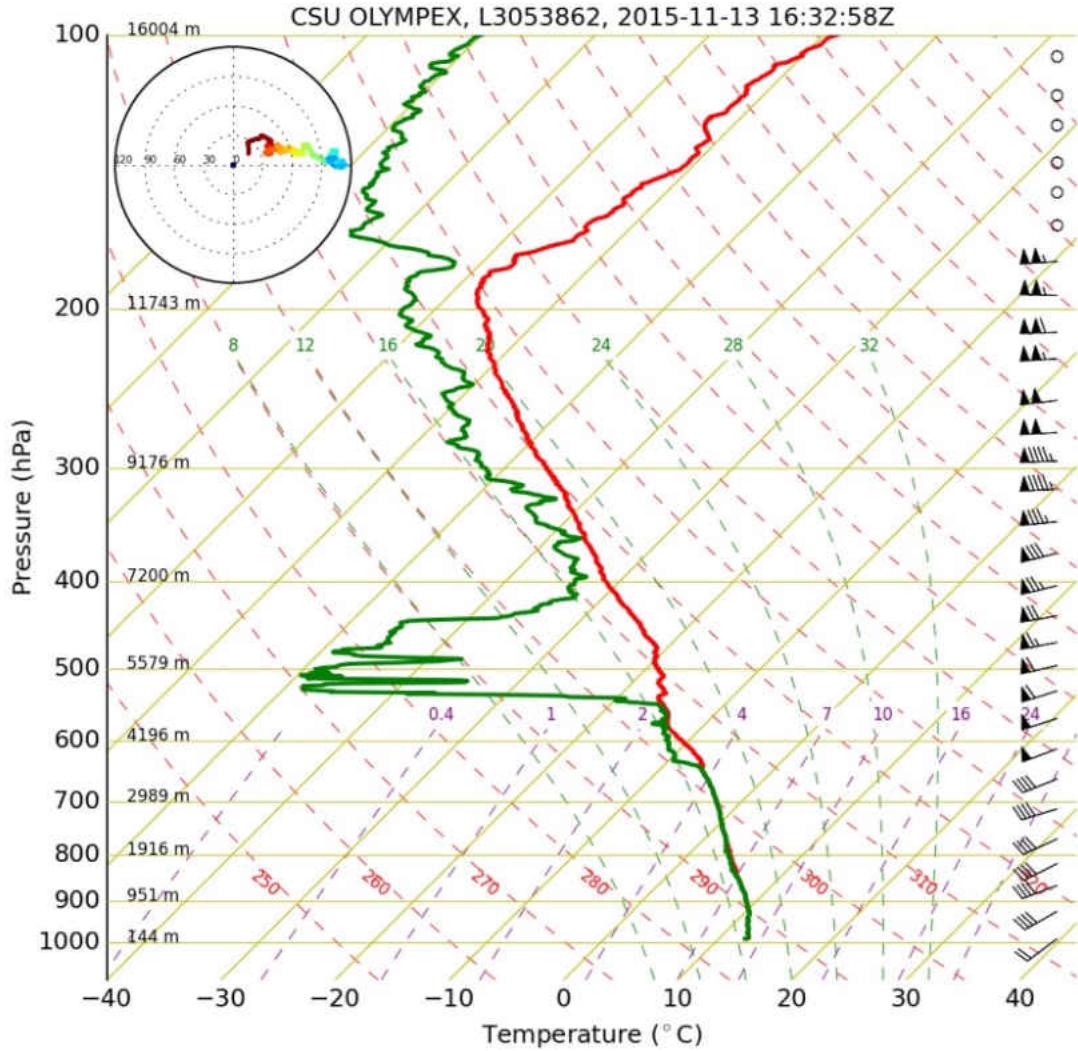


Figure 11: Sounding launched from the NASA dual-polarization S-band radar (NPOL) site on 13 Nov 2015 observed during 16:33 UTC.

The third and fourth cases occurred on 3 December 2015. Fig. 12 (Fig. 13) shows the closest NPOL base reflectivity scan in relation to the third case (fourth case). While the third case occurred in a region of zero base-tilt reflectivity due to beam blockage from the mountains, the fourth case occurred in regions of reflectivity primarily between 15-25 dBZ. The sounding launched from the NPOL site prior to both cases shows saturated conditions through the depth of the troposphere and strong south-southwesterly winds at most levels (Fig. 14).

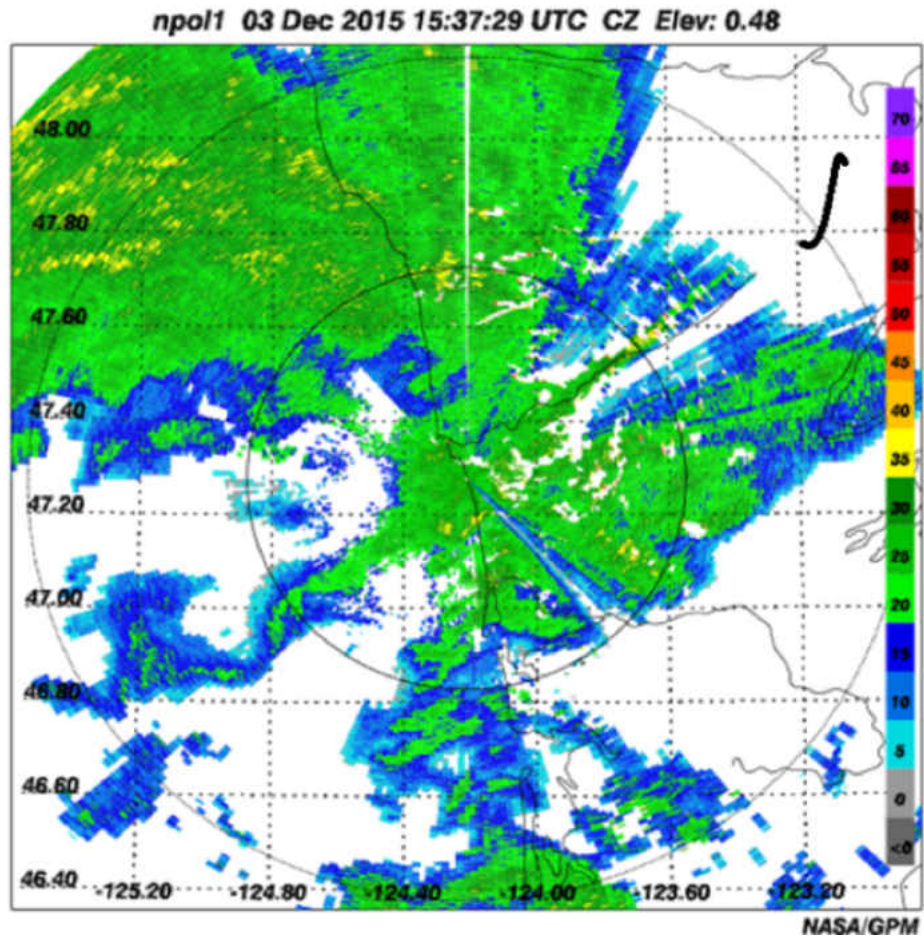


Figure 12: NASA dual-polarization S-band radar (NPOL) base reflectivity scan from 3 Dec 2015 at 15:37:29 UTC (leg start time +0:49). The black line indicates the position of the UND Citation II during (a) 15:36:40 UTC – 15:40:51 UTC.

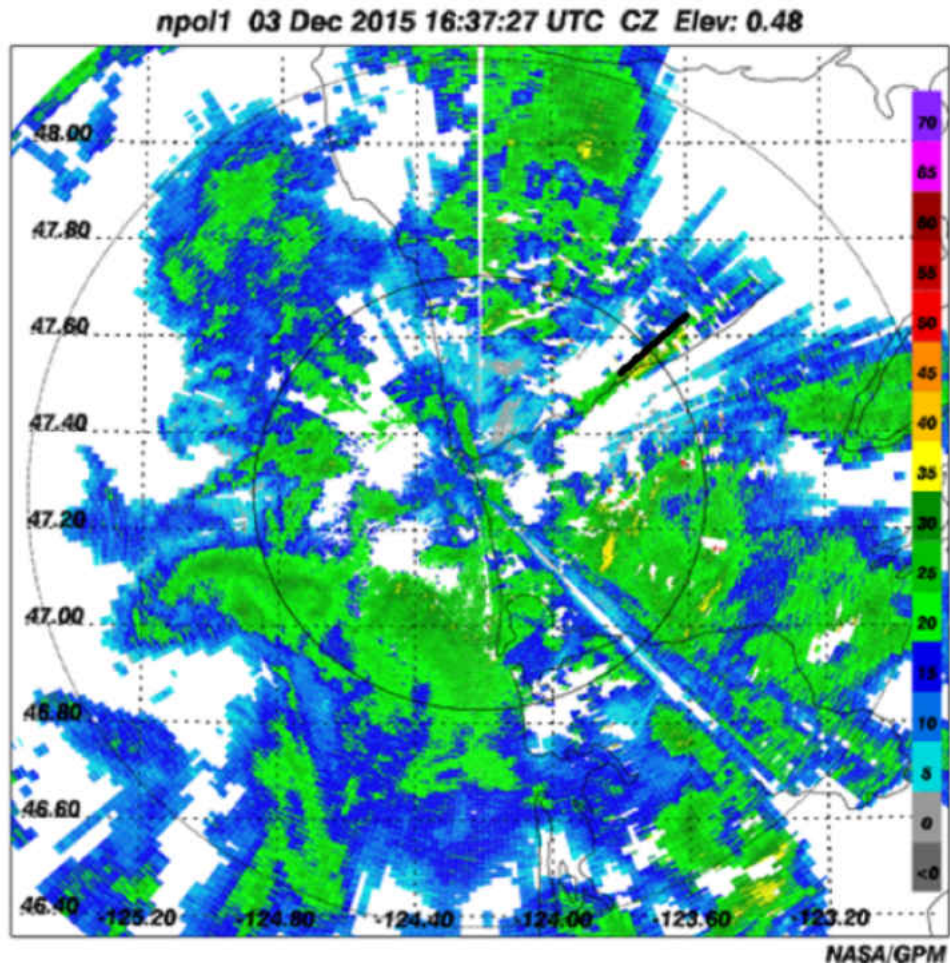


Figure 13: NASA dual-polarization S-band radar (NPOL) base reflectivity scan from 3 Dec 2015 at 16:37:27 UTC (leg end time +5:05). The black line indicates the position of the UND Citation II during 16:28:30 UTC – 16:32:22 UTC.

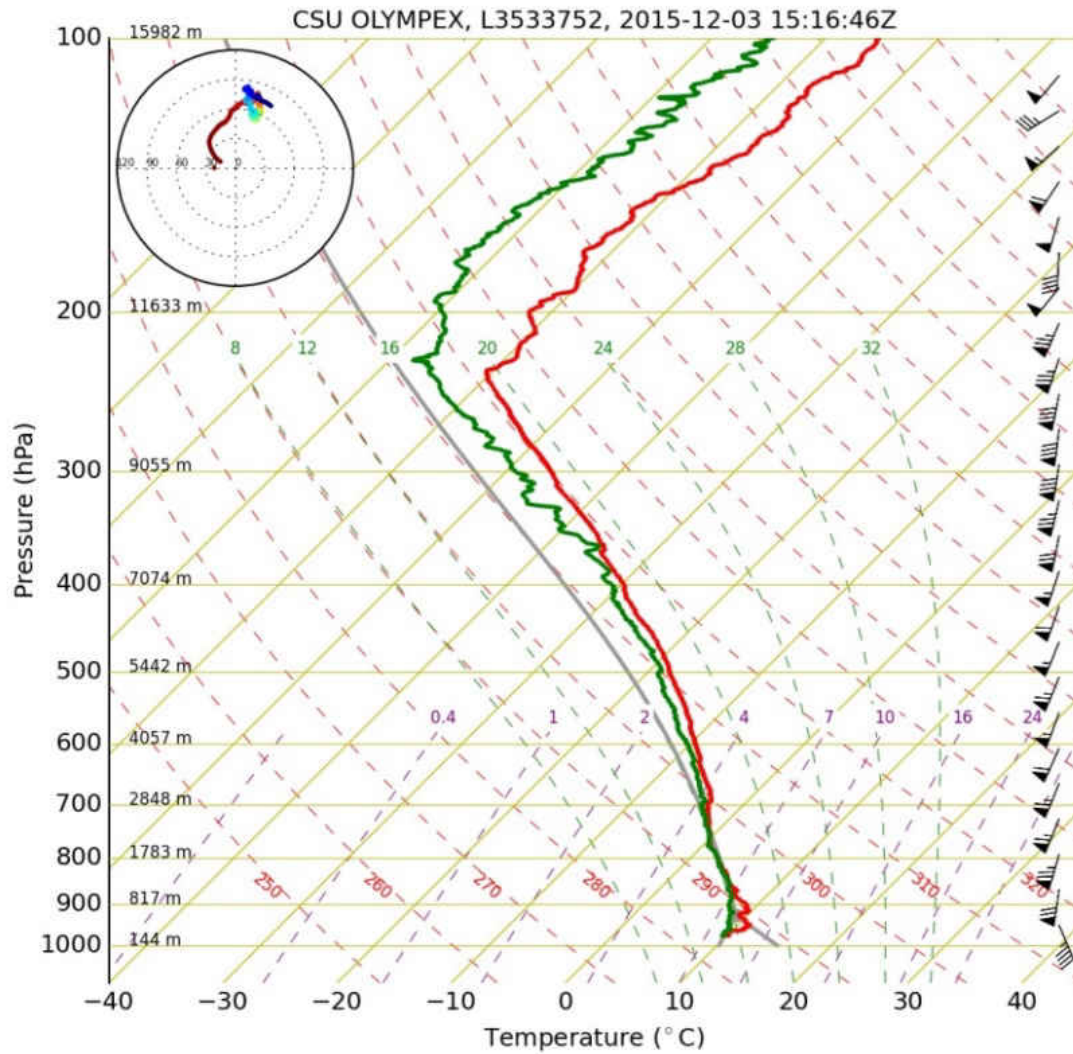


Figure 14: Sounding launched from the NASA dual-polarization S-band radar (NPOL) site on 3 Dec 2015 observed during 15:17 UTC.

Frontal

A total of eight frontal flight legs are used in this analysis (Table 2). From those eight flight legs, two representative cases are selected, as highlighted in Table 2. Fig. 15 (Fig. 16) shows the closest NPOL base reflectivity scan in relation to the first case (second case), both of which occurred on 23 November 2015, in broad regions of stratiform rain ranging in reflectivity values of 20-25 dBZ. The sounding launched from the NPOL site prior to both cases shows moist conditions throughout the depth of the troposphere with pockets of drier air from ~930 mb to ~680 mb, along with weak southwesterly winds near the surface and stronger southwesterly winds aloft (Fig. 17).

Table 2: Frontal cases. Highlighted times indicate flight legs chosen for thorough analysis.

Date	Start Time	End Time	Average Pressure Altitude
23 Nov 2015	21:06:40 UTC	21:10:54 UTC	4618 m
	21:26:40 UTC	21:31:14 UTC	4002 m
	21:35:00 UTC	21:39:49 UTC	3379 m
	21:52:30 UTC	21:57:42 UTC	2173 m
	22:00:20 UTC	22:05:50 UTC	1562 m
	22:25:50 UTC	22:31:04 UTC	2160 m
	22:41:40 UTC	22:46:20 UTC	3372 m
	22:50:00 UTC	22:54:17 UTC	3982 m

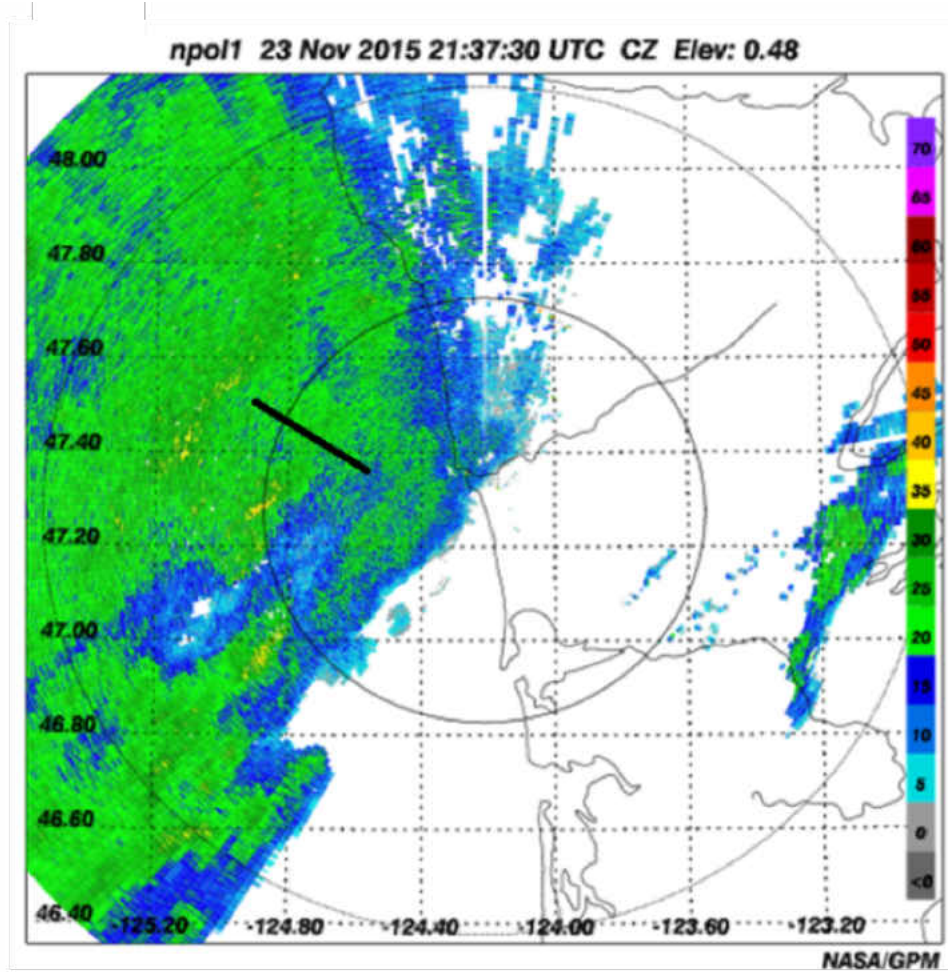


Figure 15: NASA dual-polarization S-band radar (NPOL) base reflectivity scan from 23 Nov 2015 at 21:37:30 UTC (leg end time +6:16). The black line indicates the position of the UND Citation II during (a) 21:26:40 UTC – 21:31:14 UTC.

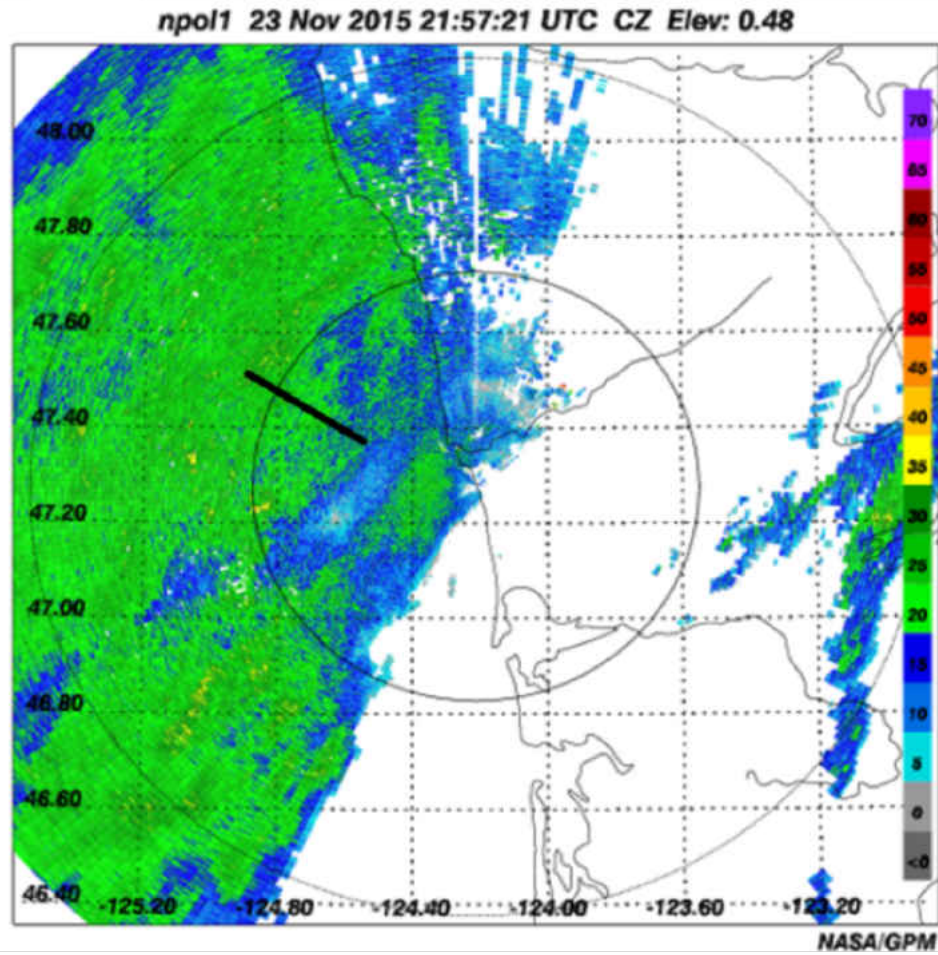


Figure 16: NASA dual-polarization S-band radar (NPOL) base reflectivity scan from 23 Nov 2015 at 21:57:21 UTC (leg start time -2:59). The black line indicates the position of the UND Citation II during 22:00:20 UTC – 22:05:50 UTC.

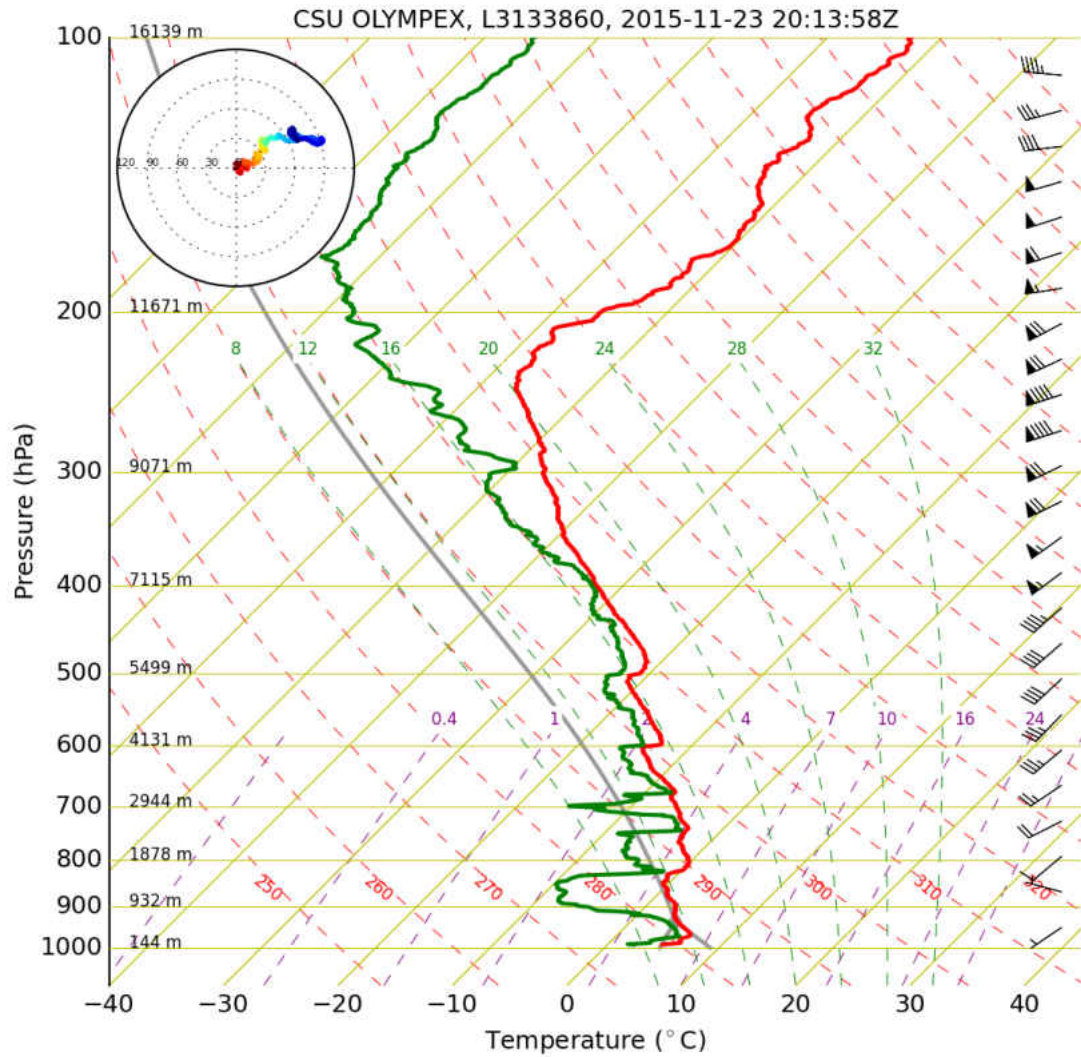


Figure 17: Sounding launched from the NASA dual-polarization S-band radar (NPOL) site on 23 Nov 2015 observed during 20:14 UTC.

Postfrontal

A total of twelve postfrontal flight legs are used in this analysis (Table 3). From those eleven flight legs, three representative cases are selected, as highlighted in Table 3. The first case occurred on 4 December 2015. Fig. 18 shows the closest NPOL base reflectivity scan in relation to the flight leg position, which occurred in regions of reflectivity primarily between 25-35 dBZ. The sounding launched from the NPOL site after the flight leg shows instability below 600 mb, with rather dry conditions aloft, and weak westerly winds at most levels (Fig. 19).

Table 3: Postfrontal cases. Highlighted times indicate flight legs chosen for thorough analysis.

Date	Start Time	End Time	Average Pressure Altitude
4 Dec 2015	13:32:08 UTC	13:36:22 UTC	3087 m
	14:37:34 UTC	14:41:48 UTC	3695 m
	14:54:34 UTC	14:58:21 UTC	4613 m
	15:08:54 UTC	15:12:35 UTC	5226 m
13 Dec 2015	16:10:00 UTC	16:14:30 UTC	3183 m
	16:55:00 UTC	16:59:58 UTC	1656 m
	17:04:10 UTC	17:08:45 UTC	2568 m
	17:13:20 UTC	17:17:31 UTC	3481 m
	17:26:40 UTC	17:30:39 UTC	4001 m
	18:18:20 UTC	18:23:00 UTC	2564 m
	18:28:20 UTC	18:32:18 UTC	3477 m

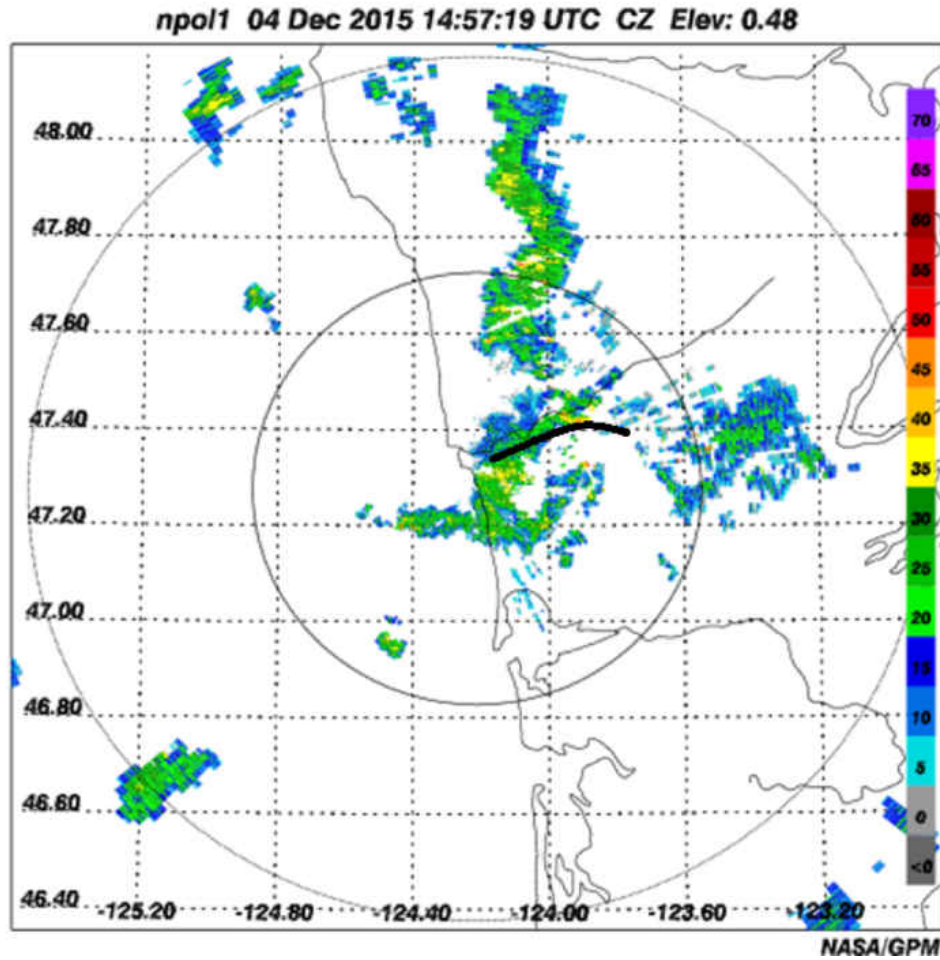


Figure 18: NASA dual-polarization S-band radar (NPOL) base reflectivity scan from 4 Dec 2015 at 14:57:19 UTC (leg start time +2:47). The black line indicates the position of the UND Citation II during 14:54:34 UTC – 14:58:21 UTC. NPOL sounding from 4 Dec 2015 observed during 15:18 UTC.

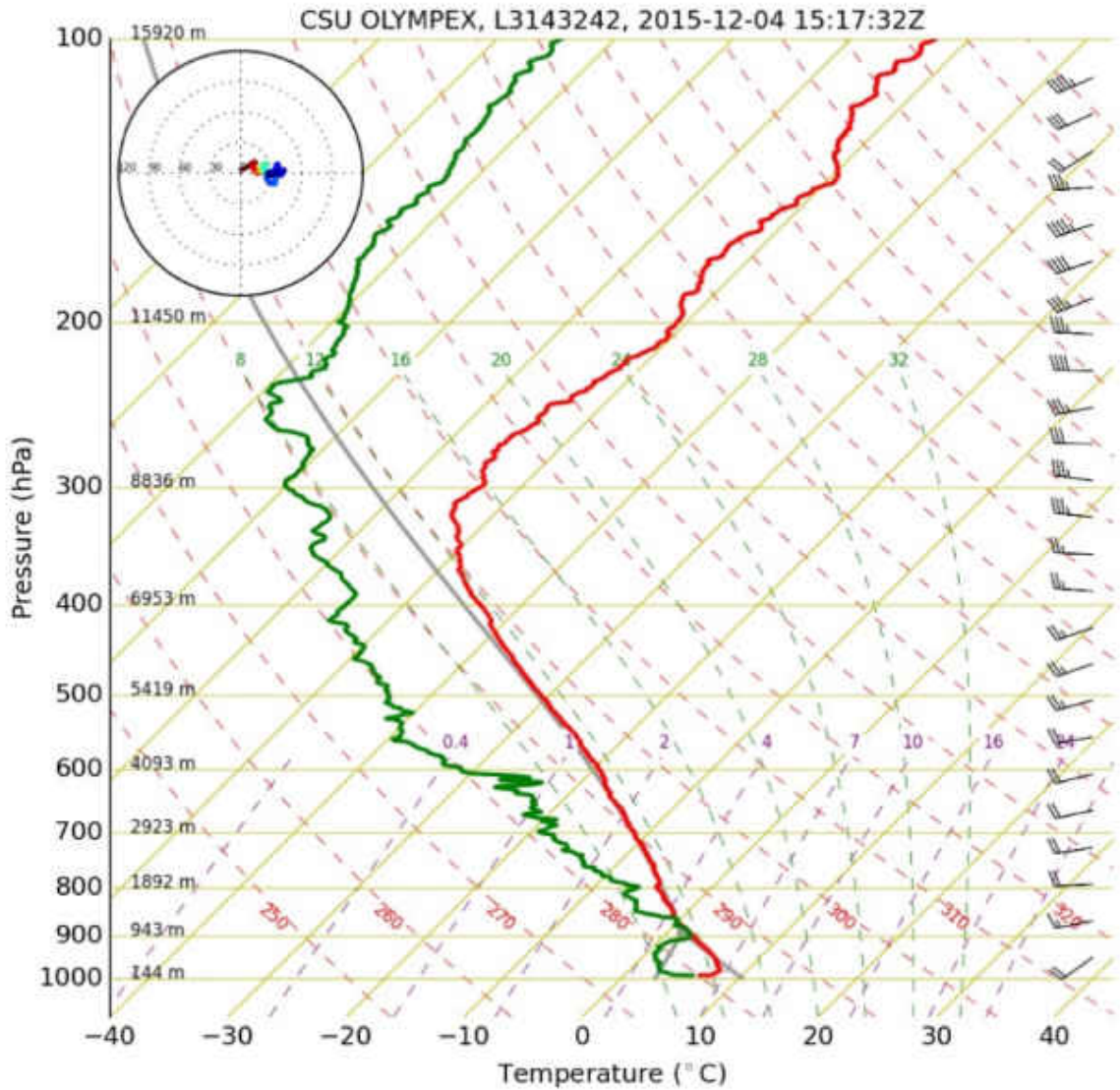


Figure 19: Sounding launched from the NASA dual-polarization S-band radar (NPOL) site on 4 Dec 2015 observed during 15:18 UTC.

The second and third cases occurred on 13 December 2015. Fig. 20 (Fig. 21) shows the closest NPOL base reflectivity scan in relation to both flight legs. Each occurred in regions of reflectivity primarily between 15-35 dBZ. The sounding launched from the NPOL site prior to both cases shows moist conditions throughout the depth of the troposphere and westerly winds at most levels (Fig. 22).

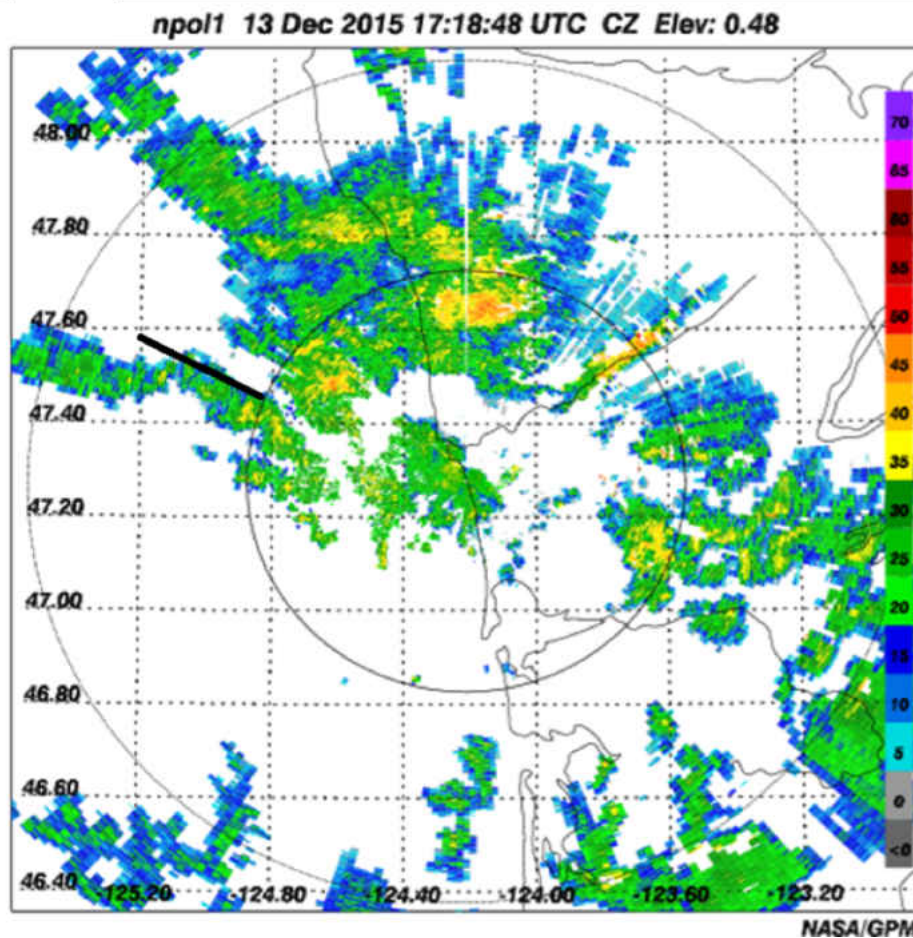


Figure 20: NASA dual-polarization S-band radar (NPOL) base reflectivity scan from 13 Dec 2015 at (a) 17:18:48 UTC (leg end time +1:17) and (b) 18:18:49 UTC (leg start time +0:29). The black line indicates the position of the UND Citation II during (a) 17:13:20 UTC – 17:17:31 UTC and (b) 18:18:20 UTC – 18:23:00 UTC.

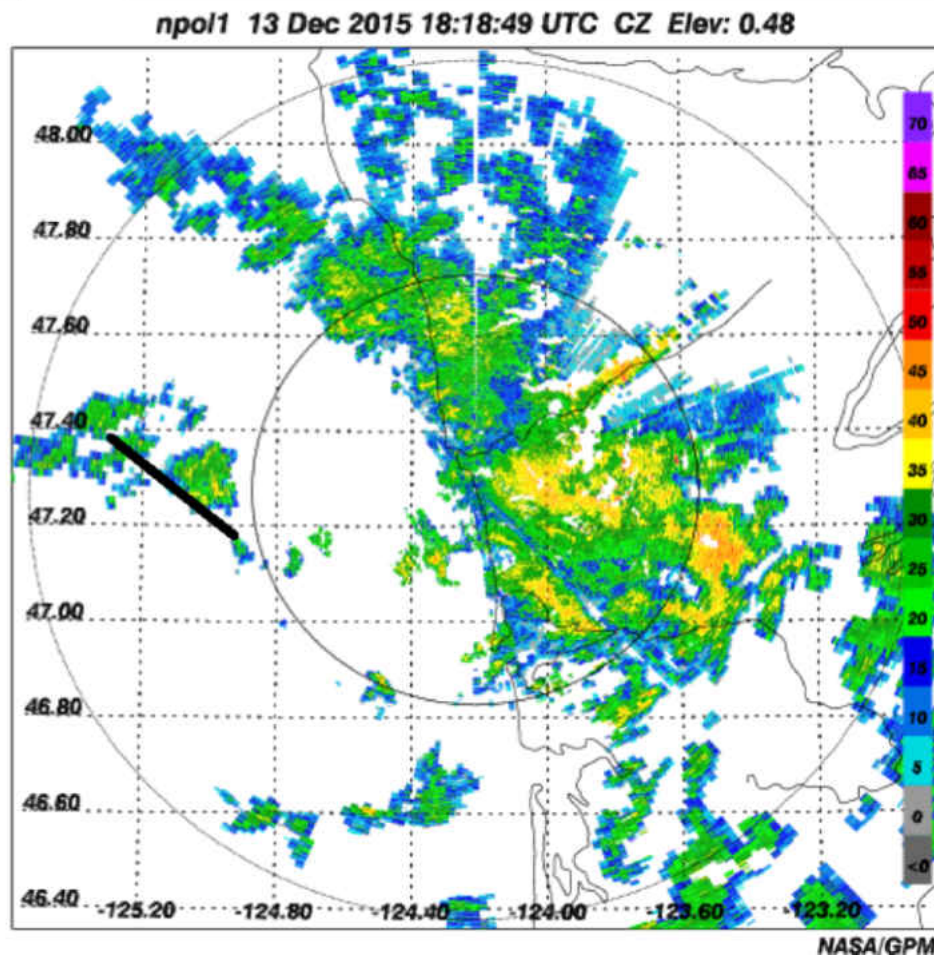


Figure 21: NASA dual-polarization S-band radar (NPOL) base reflectivity scan from 13 Dec 2015 at 18:18:49 UTC (leg start time +0:29). The black line indicates the position of the UND Citation II during 18:18:20 UTC – 18:23:00 UTC.

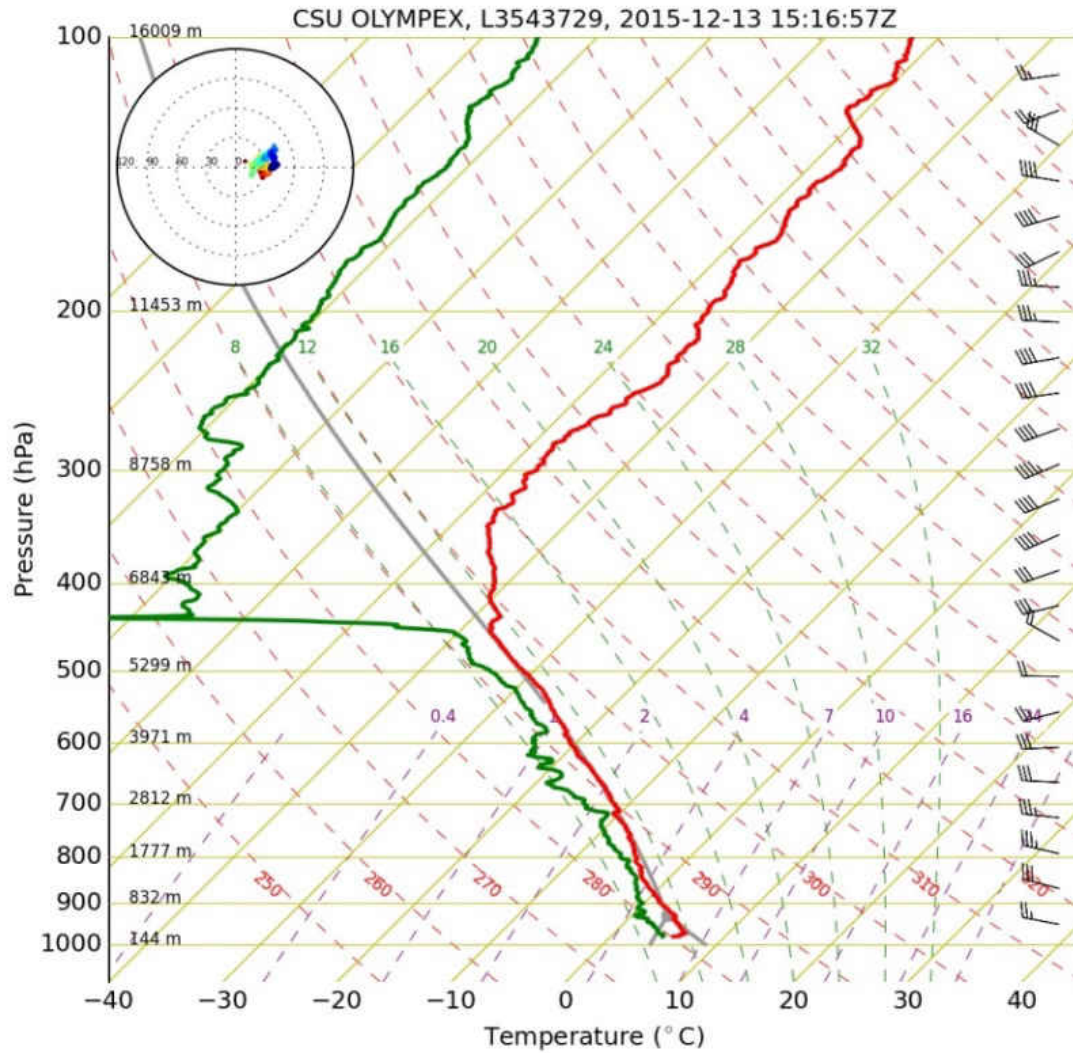


Figure 22: Sounding launched from the NASA dual-polarization S-band radar (NPOL) site on 13 Dec 2015 observed during 15:17 UTC.

CHAPTER IV

RESULTS AND DISCUSSION

Overview

The cases presented within in the previous chapter represent the flight legs from each sector that are used in this analysis. Of those cases, a select few from each sector are chosen to provide a representative view of clustering for that specific sector. A counts series, pair correlation, and spectral density plot are shown for each selected case. Additionally, derived measurements of particle size outlined in Chapter II and other parameters observed in-situ (pressure altitude, temperature, and turbulence) are presented to quantitatively determine whether any trends in clustering exist within each sector. This chapter also discusses similarities and differences found between the synoptic regimes in regards to the correlations found between the max pair correlation and parameters described previously. Lastly, trends in spectral density between each sector are noted.

Prefrontal

While two prefrontal flights are used in this analysis, the 13 November 2015 flight experienced warmer temperatures with five flight legs in above freezing conditions (i.e. rain). To minimize biases in statistics, prefrontal flight legs that occurred in rain are separated from those that occurred in ice. This provides an opportunity to compare the distributions of rain and ice to determine whether any similarities or differences exist.

Prefrontal Rain

The counts series for the first 13 November 2015 case (Fig. 23) shows the number of counts is less than 30 for most of the flight leg, with higher counts near 2, 4, and 29 km. The average count is 9.0 for the entire 30 km flight leg. The corresponding pair correlation (Fig. 23) has a maximum value of 1.46 and decreases as the lag increases until it reaches 1 km, where a slight increase in pair correlation is observed before decreasing again. This flight leg is chosen because its max pair correlation value is the largest observed for rain cases and provides an example of how low counts affect the max pair correlation. The spectral density (Fig.23) shows values near $10^{-3} \text{ m}^2 \text{ s}$ for lower frequencies (i.e. larger distances, as previously discussed in Chapter II), decreasing to $10^{-4} \text{ m}^2 \text{ s}$ before the signal resembles noise at higher frequencies. There are no substantial minima or maxima observed during this flight leg.

In comparison, the counts series for the second 13 November 2015 case (Fig. 24) shows the number of counts generally decreases throughout the duration of the leg. The average count is 58.0, which is substantially higher than for the previous leg. The corresponding pair correlation (Fig. 24) has a max value of 0.34 and is nearly constant for most lags. This flight leg is chosen because it provides a representative view of clustering for flight legs with low counts. The spectral density (Fig. 24) shows values near $10^{-3} \text{ m}^2 \text{ s}$ for lower frequencies, decreasing to $10^{-6} \text{ m}^2 \text{ s}$ before the signal resembles noise at higher frequencies. There are no substantial minima or maxima observed during this flight leg.

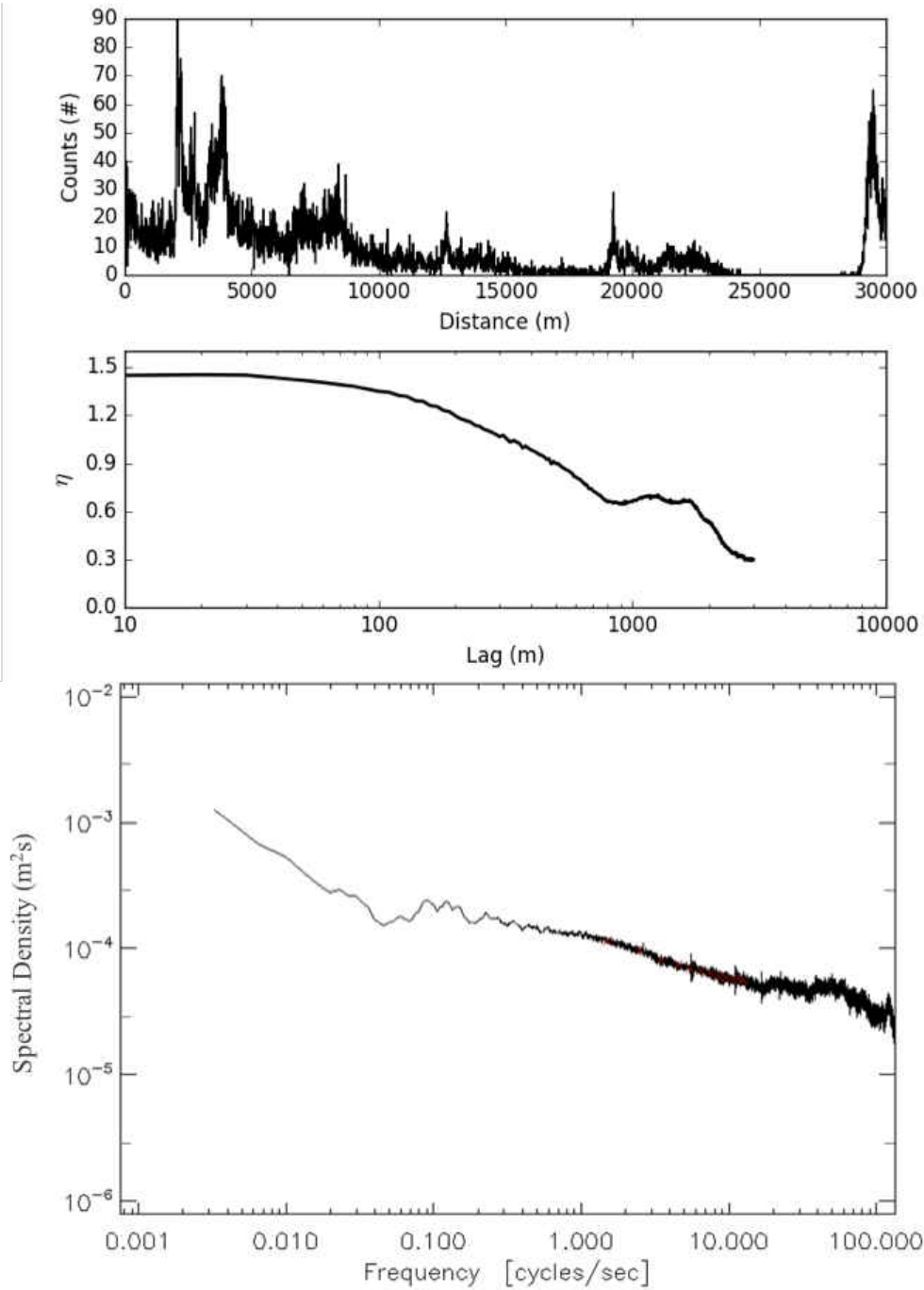


Figure 23: Counts series (top image) for the 13 Nov 2015 flight during 16:28:30 UTC-16:33:34 UTC. Data represent the number of counts observed per 10 meters. Pair correlation (middle image) derived using the counts series above. Maximum lag is one-tenth of the total flight leg distance. Spectral density (bottom image) of the derived spatial series during 16:28:30 UTC-16:33:34 UTC.

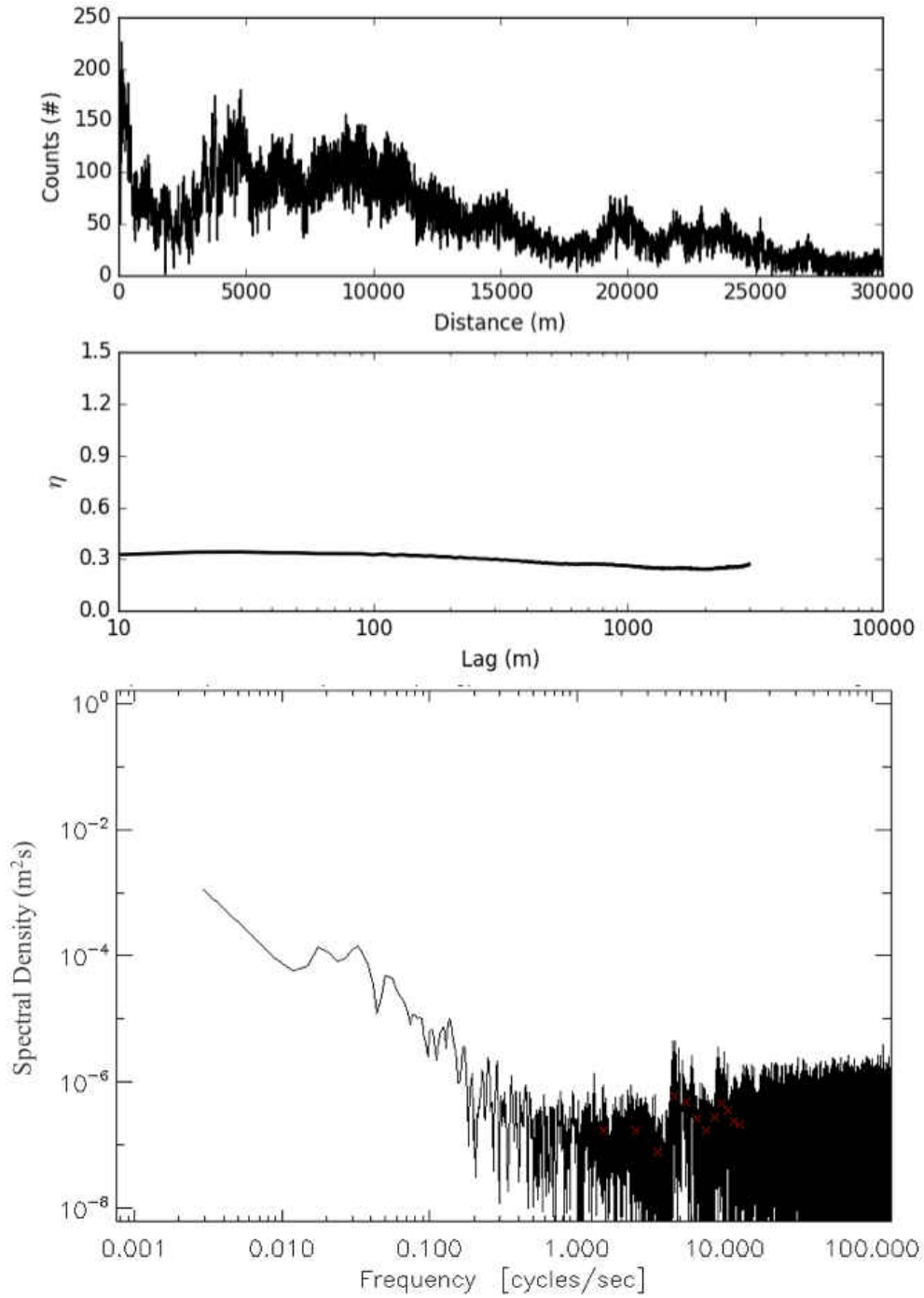


Figure 24: Counts series (top image) for the 13 Nov 2015 flight during 17:25:30 UTC-17:31:10 UTC. Data represents the number of counts observed per 10 meters. Pair correlation (middle image) derived using the counts series above. Maximum lag is one-tenth of the total flight leg distance. Spectral density (bottom image) of the derived spatial series during 17:25:30 UTC-17:31:10 UTC.

All prefrontal rain flight leg averages for derived parameters and parameters observed in-situ are found in Table 4. Scatter plots of these parameters compared to the max pair correlation are seen in Fig. 25, which also includes a linear best fit equation and correlation coefficient, r .

Table 4: Prefrontal rain flight leg averages (excluding max pair correlation). Highlighted times indicate flight legs chosen for a more thorough analysis.

Pressure Altitude	Temperature	Counts	Turbulence	Mean Volume Diameter	Mean Diameter	Max Pair Correlation
m	°C	#	$m^{2/3} s^{-1}$	μm	μm	#
13 Nov 2015						
16:28:30-16:33:34 UTC	4	9.0	0.025	2817	1236	1.46
16:56:40-17:01:55 UTC	5	41.2	0.047	385	577	0.39
17:25:30-17:31:10 UTC	9	58.0	0.065	585	964	0.34
17:35:30-17:40:47 UTC	5	44.0	0.049	2586	741	0.82
18:10:00-18:14:44 UTC	6	5.7	0.069	2310	827	1.30

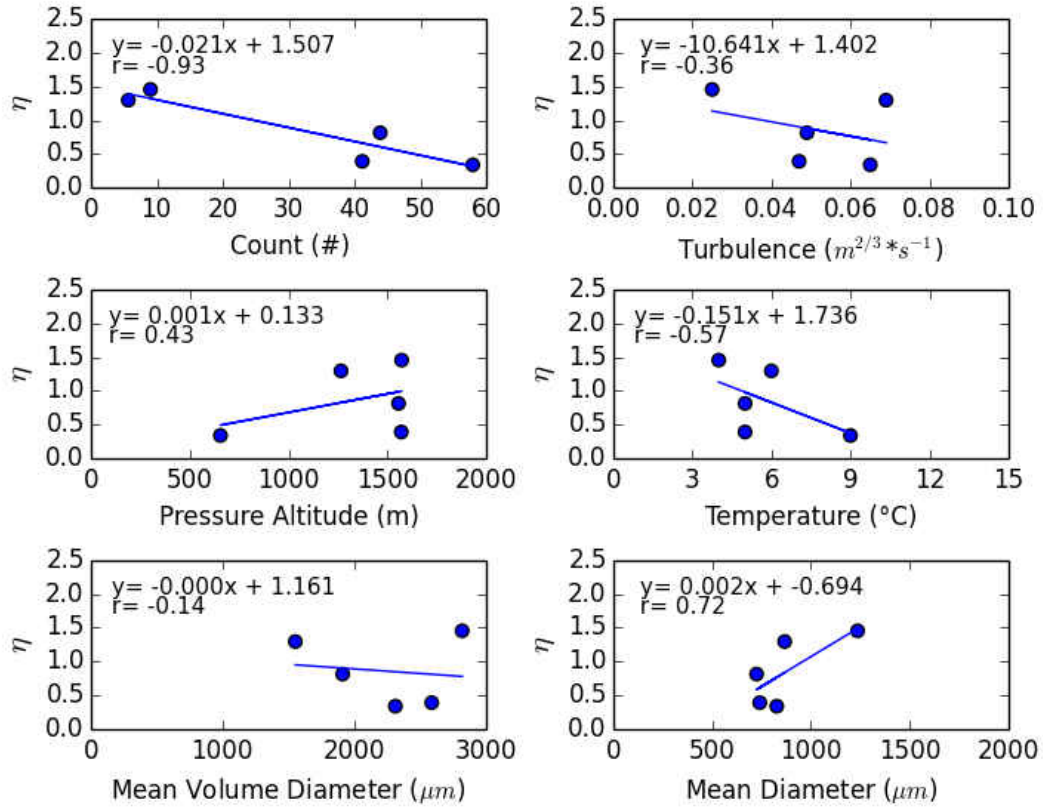


Figure 25: Prefrontal flight leg parameter averages compared to the max pair correlation. All flight legs occurred in above freezing conditions (i.e. rain). Each plot includes a linear best fit equation and correlation coefficient, r .

Prefrontal Ice

The counts series for the first 3 December 2015 case (Fig. 26) shows the number of counts is relatively high for the duration of the flight and has an average count of 198.5. The corresponding pair correlation (Fig. 26) has a max value of 0.05 and is nearly constant for most lags before it trends towards zero around 3 km. This flight leg is chosen because it provides a representative view of clustering for flight legs with high counts. The spectral density (Fig. 26) shows values near $10^{-5} \text{ m}^2 \text{ s}$ for lower frequencies, decreasing to $10^{-8} \text{ m}^2 \text{ s}$ before the signal resembles noise at higher frequencies. A noticeable minimum occurs near 0.020 s^{-1} ($\sim 9 \text{ km}$).

In comparison, the counts series for the second 3 December 2015 case (Fig. 27) shows the number of counts is less than 10 for most of the leg, with a small region of higher counts (up to 30) between 14-17 km. The corresponding pair correlation (Fig. 27) has a max value of 1.05 and decreases toward zero at long lags. This flight leg is chosen because it provides a representative view of clustering for flight legs with low counts. The spectral density (Fig. 27) shows values near $10^0 \text{ m}^2 \text{ s}$ for lower frequencies, decreasing to $10^{-4} \text{ m}^2 \text{ s}$ before the signal resembles noise at higher frequencies. There are no substantial minima or maxima observed during this flight leg.

All prefrontal ice flight leg averages for derived parameters and parameters observed in-situ are found in Table 5. Corresponding scatter plots of these parameters compared to the max pair correlation are seen in Fig. 28, which also includes a linear best fit equation and correlation coefficient, r .

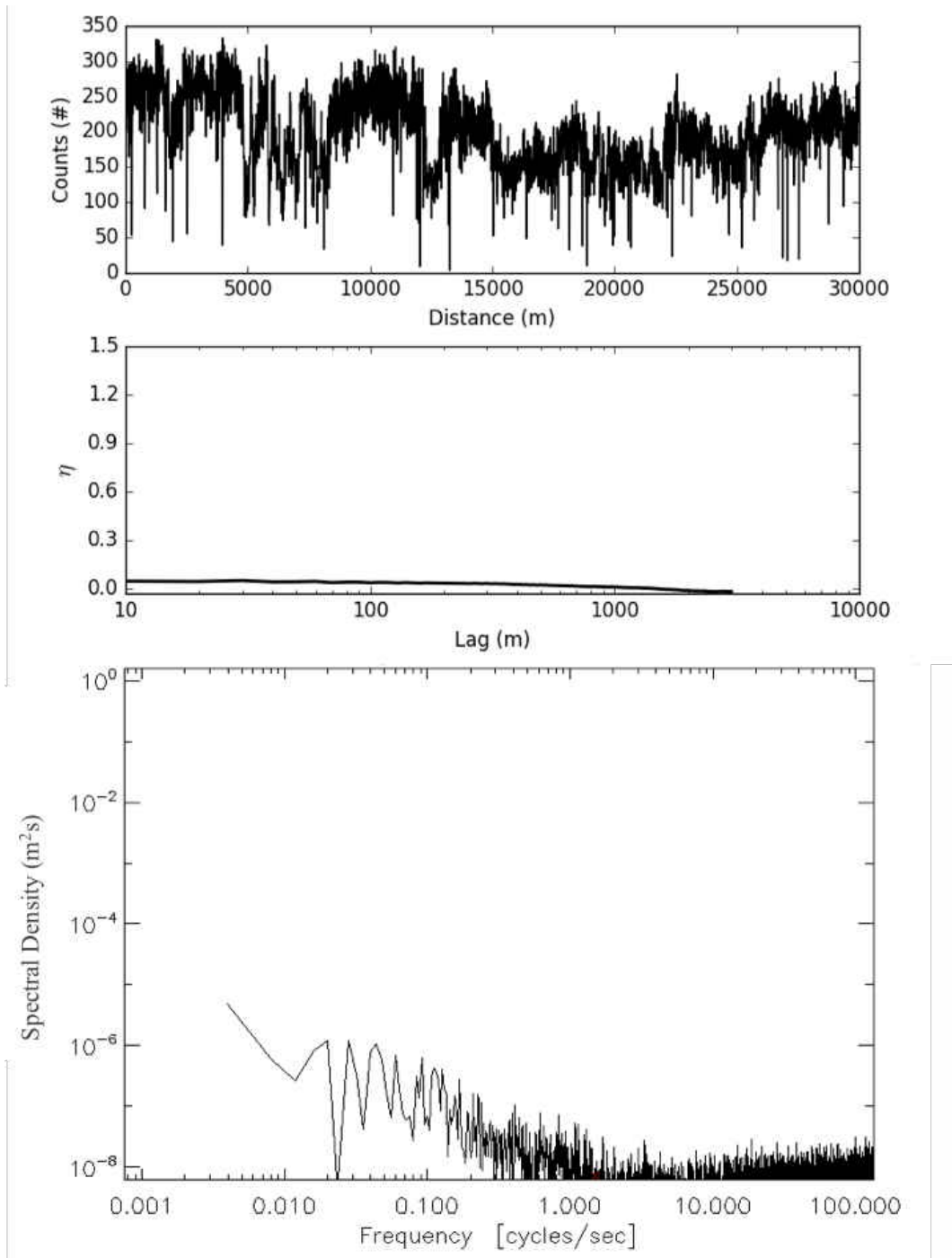


Figure 26: Counts series (top image) for the 3 Dec 2015 flight during 15:36:40 UTC-15:40:51 UTC. Data represents the number of counts observed per 10 meters. Pair correlation (middle image) derived using the counts series above. Maximum lag is one-tenth of the total flight leg distance. Spectral density (bottom image) of the derived spatial series during 15:36:40 UTC-15:40:51 UTC.

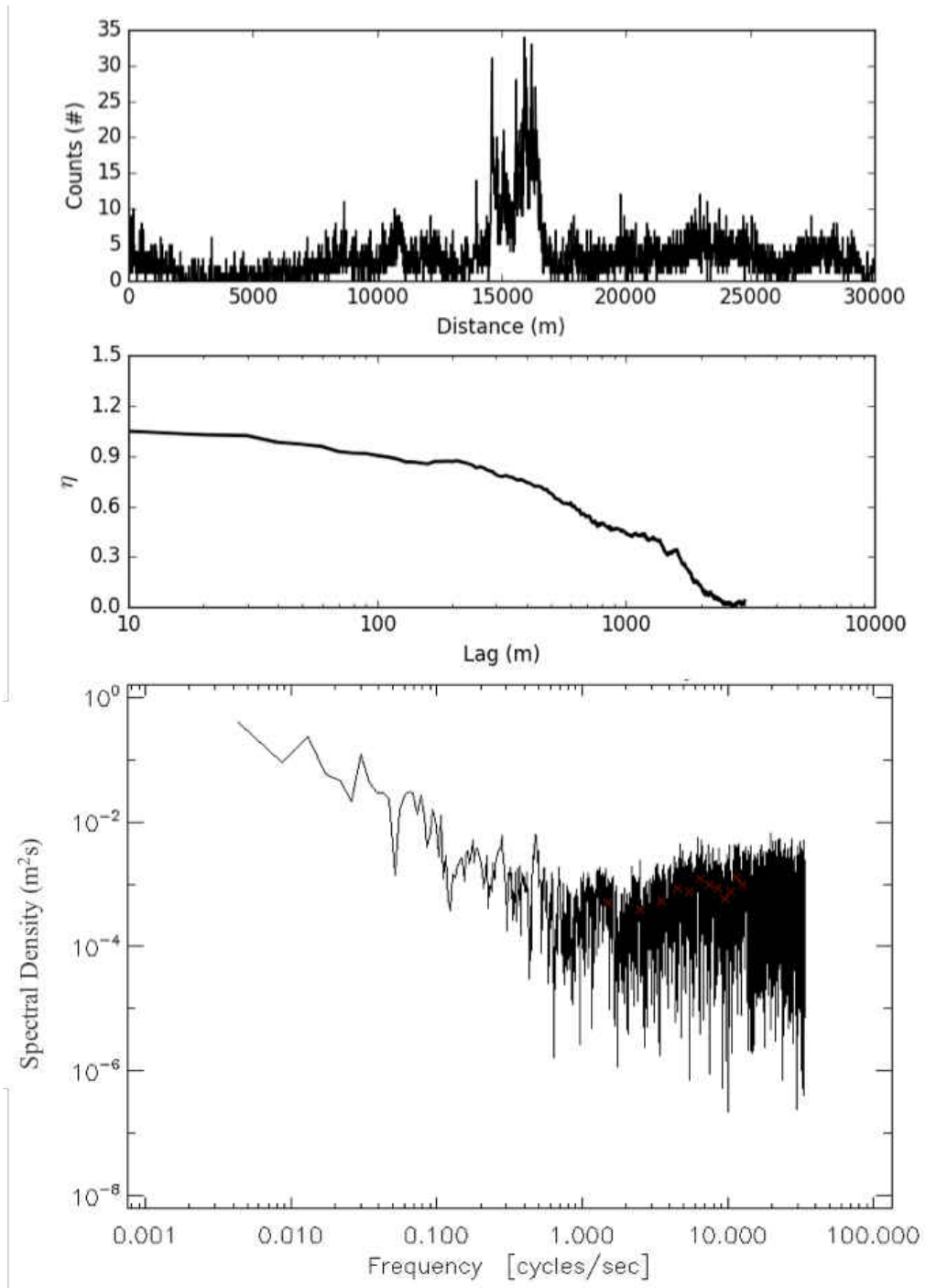


Figure 27: Counts series (top image) for the 3 Dec 2015 flight during 16:28:30 UTC-16:32:22 UTC (Top). Data represents the number of counts observed per 10 meters. Pair correlation (middle image) derived using the counts series above. Maximum lag is one-tenth of the total flight leg distance. Spectral density (bottom image) of the derived spatial series during 16:28:30 UTC-16:32:22 UTC.

Table 5: Prefrontal ice flight leg averages (excluding max pair correlation). Highlighted times indicate flight legs chosen for a more thorough analysis.

Pressure Altitude	Temperature	Counts	Turbulence	Mean Volume Diameter	Mean Diameter	Max Pair Correlation
m	°C	#	$m^{2/3}s^{-1}$	μm	μm	#
13 Nov 2015						
15:15:50-15:19:33 UTC	-1	3.9	0.024	758	801	1.04
16:11:40-16:15:55 UTC	-4	125.5	0.044	4929	1129	0.11
3 Dec 2015						
14:38:20-14:41:52 UTC	-20	129.3	0.052	4127	1383	0.06
15:03:20-15:07:18 UTC	-12	69.6	0.085	6322	2700	0.08
15:36:40-15:40:51 UTC	-6	198.5	0.126	6890	1878	0.05
16:17:10-16:21:22 UTC	-12	14.2	0.046	5134	2688	0.39
16:28:30-16:32:22 UTC	-21	3.5	0.022	1506	1041	1.05
16:40:00-16:44:01 UTC	-11	28.5	0.041	3764	1635	0.35

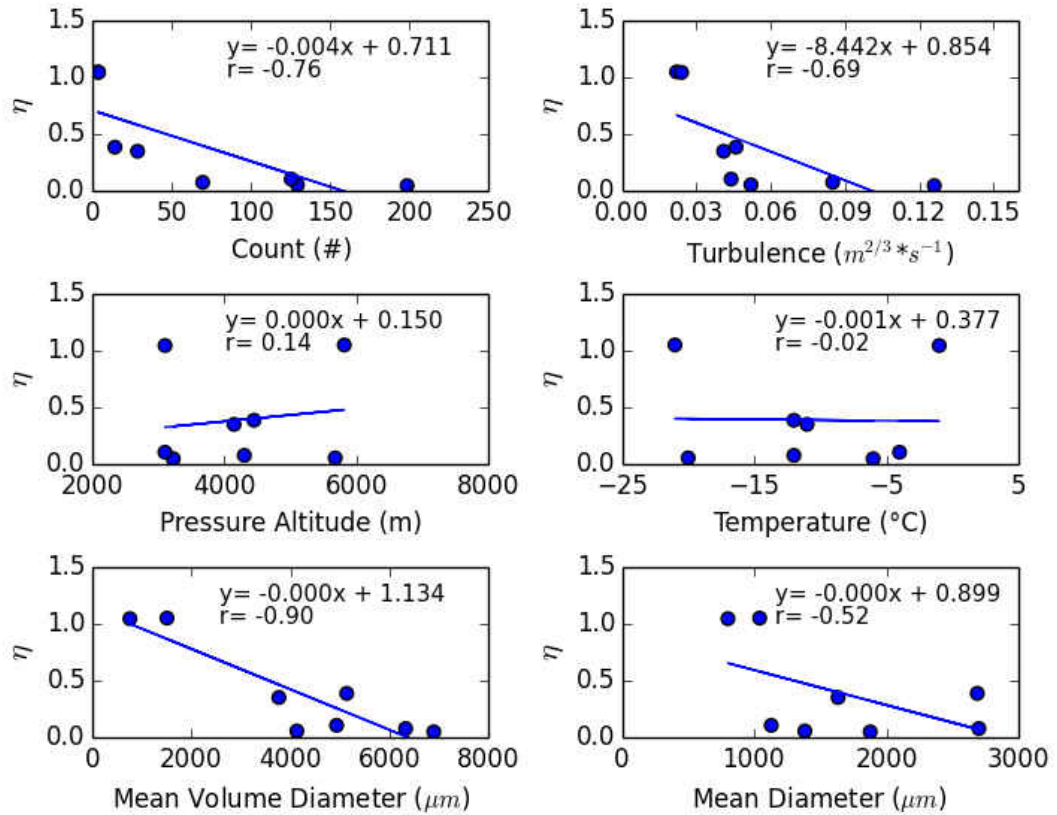


Figure 28: Prefrontal flight leg parameter averages compared to the max pair correlation. All flight legs occurred in below freezing conditions (i.e. ice). Each plot includes a linear best fit equation and correlation coefficient, r .

Frontal

Legs for the frontal sector are chosen from the 23 November 2018 flight. Since the counts are fairly uniform, legs are chosen based on temperature. The counts series for the first case (Fig. 29) shows the number of counts are fairly consistent and has an average count of 67.5. However, peaks in counts did occur near 7, 18, and 27 km. The corresponding pair correlation (Fig. 29) has a max value of 0.06 and is nearly constant for most lags. This flight leg is chosen because it provides a representative view of clustering for legs sampled at colder temperatures (higher in the cloud) on this flight. The spectral density (Fig. 29) shows values near $10^{-4} \text{ m}^2 \text{ s}$ for lower frequencies, decreasing to $10^{-7} \text{ m}^2 \text{ s}$ before the signal resembles noise at higher frequencies. There are no substantial minima or maxima observed during this flight leg.

The counts series for the second case (Fig. 30) shows the number of counts generally decreases throughout the flight and has an average count of 49.1. The corresponding pair correlation (Fig. 30) has a max value of 0.05 and is nearly constant for most lags. This flight leg is chosen because it provides a representative view of clustering for legs sampled at warmer temperatures (lower in cloud) on this flight. Much like the colder leg, the spectral density (Fig. 30) shows values near $10^{-4} \text{ m}^2 \text{ s}$ for lower frequencies, decreasing to $10^{-7} \text{ m}^2 \text{ s}$ before the signal resembles noise at higher frequencies. There are no substantial minima or maxima observed during this flight leg.

All frontal flight leg averages for derived parameters and parameters observed in-situ are found in Table 6. Corresponding scatter plots of these parameters compared to the max pair correlation are seen in Fig. 31, which also includes a linear best fit equation and correlation coefficient, r .

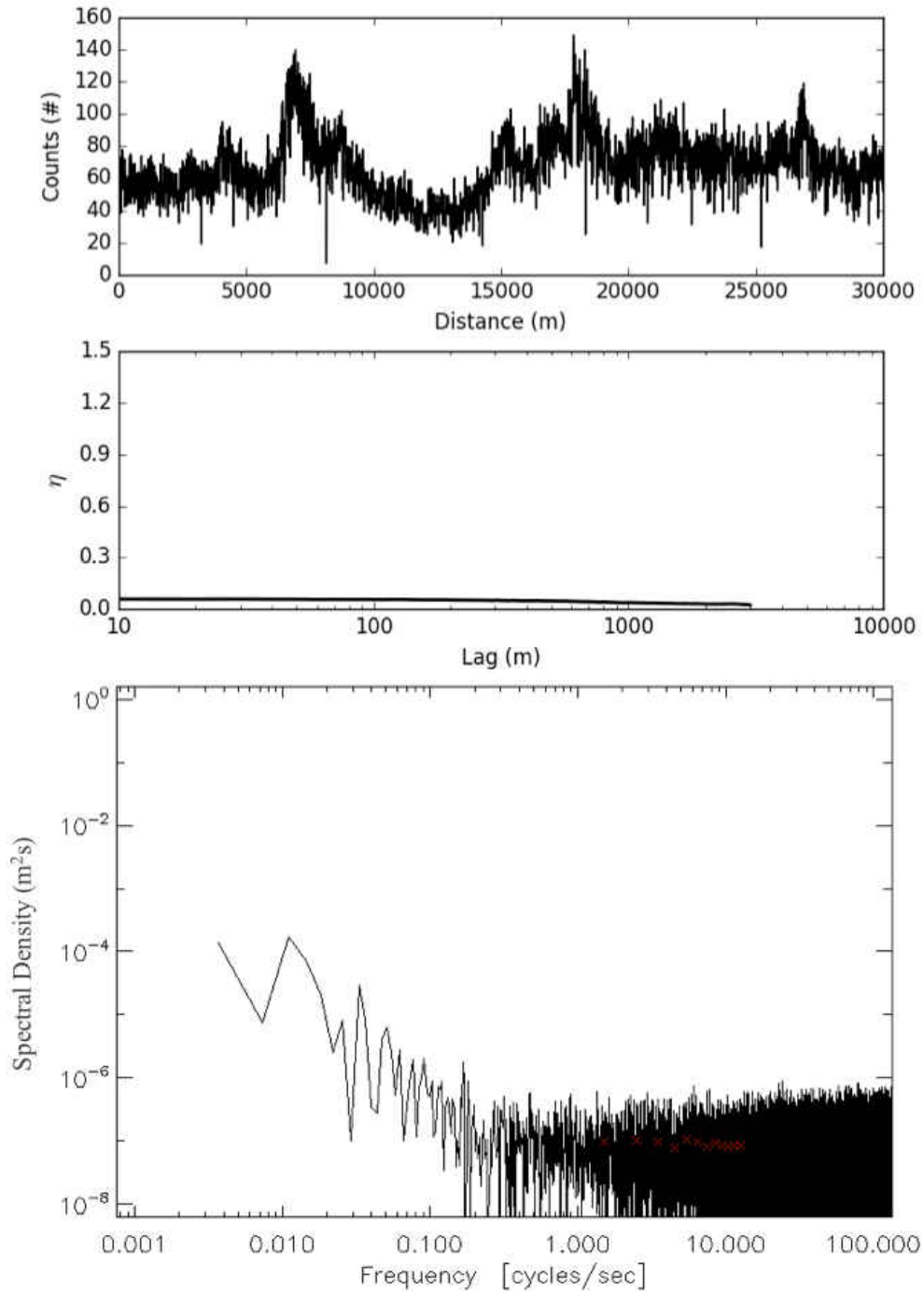


Figure 29: Counts series (top image) for the 23 Nov 2015 flight during 21:26:40 UTC-21:31:14 UTC. Data represents the number of counts observed per 10 meters. Pair correlation (middle image) derived using the counts series above. Maximum lag is one-tenth of the total flight leg distance. Spectral density (bottom image) of the derived spatial series during 21:26:40 UTC-21:31:14 UTC.

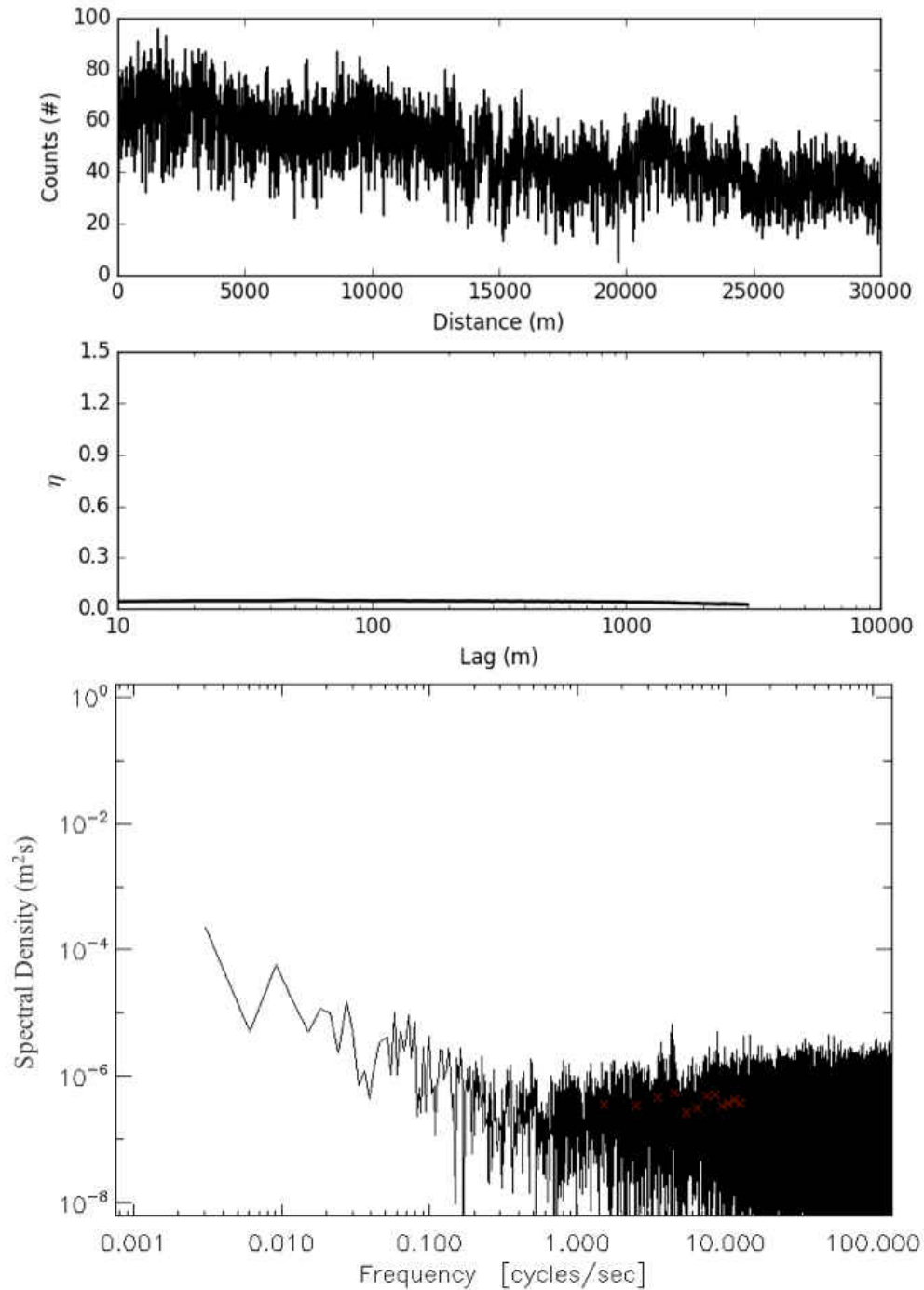


Figure 30: Counts series (top image) for the 23 Nov 2015 flight during 22:00:20 UTC-22:05:50 UTC. Data represents the number of counts observed per 10 meters. Pair correlation (middle image) derived using the counts series above. Maximum lag is one-tenth of the total flight leg distance. Spectral density (bottom image) of the derived spatial series during 22:00:20 UTC-22:05:50 UTC.

Table 6: Frontal flight leg averages (excluding max pair correlation). Highlighted times indicate flight legs chosen for a more thorough analysis.

Pressure Altitude	Temperature	Counts	Turbulence	Mean Volume Diameter	Mean Diameter	Max Pair Correlation
m	°C	#	$m^{2/3}s^{-1}$	μm	μm	#
23 Nov 2015						
21:06:40-21:10:54 UTC	-16	55.1	0.025	2236	996	0.13
21:26:40-21:31:14 UTC	-13	67.5	0.027	2444	998	0.06
21:35:00-21:39:49 UTC	-9	68.1	0.047	2623	1029	0.05
21:52:30-21:57:42 UTC	-4	72.2	0.025	3024	1182	0.10
22:00:20-22:05:50 UTC	-2	49.1	0.045	3295	1474	0.05
22:25:50-22:31:04 UTC	-5	59.4	0.053	4028	1760	0.16
22:41:40-22:46:20 UTC	-11	87.1	0.034	3511	1438	0.02
22:50:00-22:54:17 UTC	-14	126.0	0.030	3494	1182	0.04

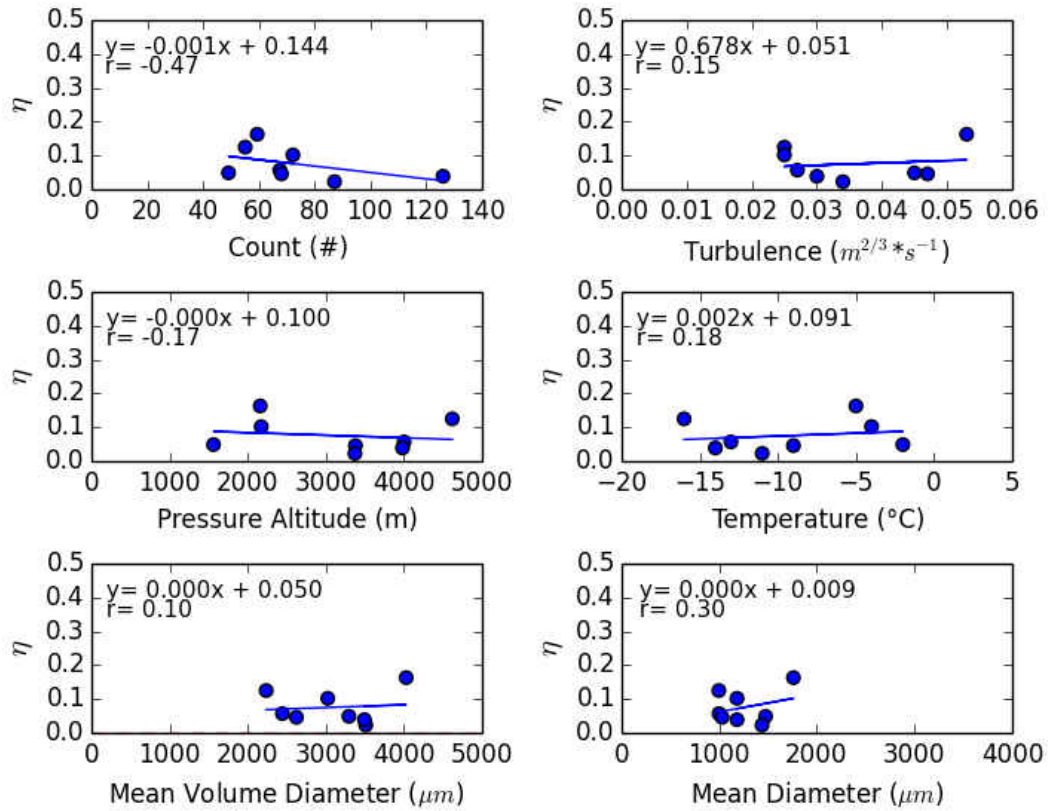


Figure 31: Frontal flight leg parameter averages compared to the max pair correlation. Each plot includes a linear best fit equation and correlation coefficient, r.

Postfrontal

The counts series for the 4 December 2015 case (Fig. 32) shows the number of counts fluctuates during the first half of the flight before becoming more consistent for the remainder. The average count is 74.6 for the entire flight leg. The corresponding pair correlation (Fig. 32) has a max value of 0.38 and decreases toward zero as the lag increases, with a slight increase near 1 km. This flight leg is chosen because it provides a representative view of clustering for flight legs with moderate counts. The spectral density (Fig. 32) shows values near $10^{-5} \text{ m}^2 \text{ s}$ for lower frequencies, decreasing to $10^{-7} \text{ m}^2 \text{ s}$ before the signal resembles noise at higher frequencies. A noticeable minimum occurs near 0.020 s^{-1} ($\sim 9 \text{ km}$).

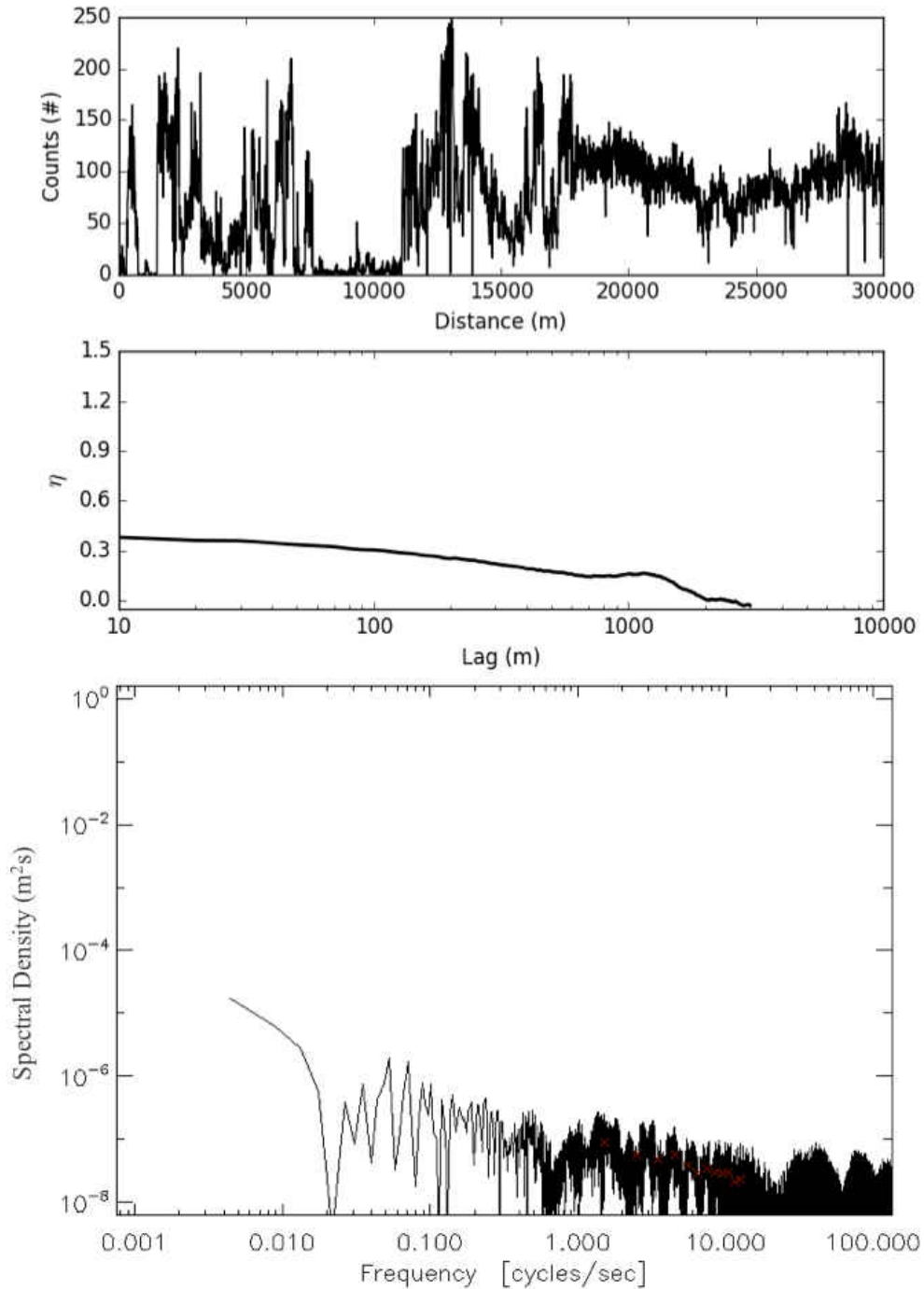


Figure 32: Counts series (top image) for the 4 Dec 2015 flight during 14:54:34 UTC-14:58:21 UTC. Data represents the number of counts observed per 10 meters. Pair correlation (middle image) derived using the counts series above. Maximum lag is one-tenth of the total flight leg distance. Spectral density (bottom image) of the derived spatial series during 14:54:34 UTC-14:58:21 UTC.

The counts series for the first 13 December 2015 case (Fig. 33) shows the number of counts fluctuates for most of the flight before becoming more consistent near 18 km and has an average count of 178.8. The corresponding pair correlation (Fig. 33) has a max value of 0.11 and nearly constant for most lags. This flight leg is chosen because it provides a representative view of clustering for flight legs with high counts. The spectral density (Fig. 33) shows values near $10^{-5} \text{ m}^2 \text{ s}$ for lower frequencies, decreasing to $10^{-8} \text{ m}^2 \text{ s}$ before the signal resembles noise at higher frequencies. Two noticeable minima occur near 0.020 s^{-1} ($\sim 9 \text{ km}$) and 0.090 s^{-1} ($\sim 2 \text{ km}$).

In comparison, the counts series for the second 13 December 2015 case (Fig. 34) shows the number of counts is relatively low and consistent during the beginning of the flight before it begins to increase and fluctuate for the remainder of the flight. The average count is 82.9 for the entire leg. The corresponding pair correlation (Fig. 34) has a max value of 0.35 and nearly constant for most lags. This flight leg is chosen because its average count and max pair correlation are similar to the 4 December 2015 case. The spectral density (Fig. 34) shows values near $10^{-3} \text{ m}^2 \text{ s}$ for lower frequencies, decreasing to $10^{-6} \text{ m}^2 \text{ s}$ before the signal resembles noise at higher frequencies. A noticeable minimum occurs near 0.100 s^{-1} ($\sim 1 \text{ km}$).

All postfrontal flight leg averages for derived parameters and parameters observed in-situ are found in Table 7. Corresponding scatter plots of these parameters compared to the max pair correlation are seen in Fig. 35, which also includes a linear best fit equation and correlation coefficient, r .

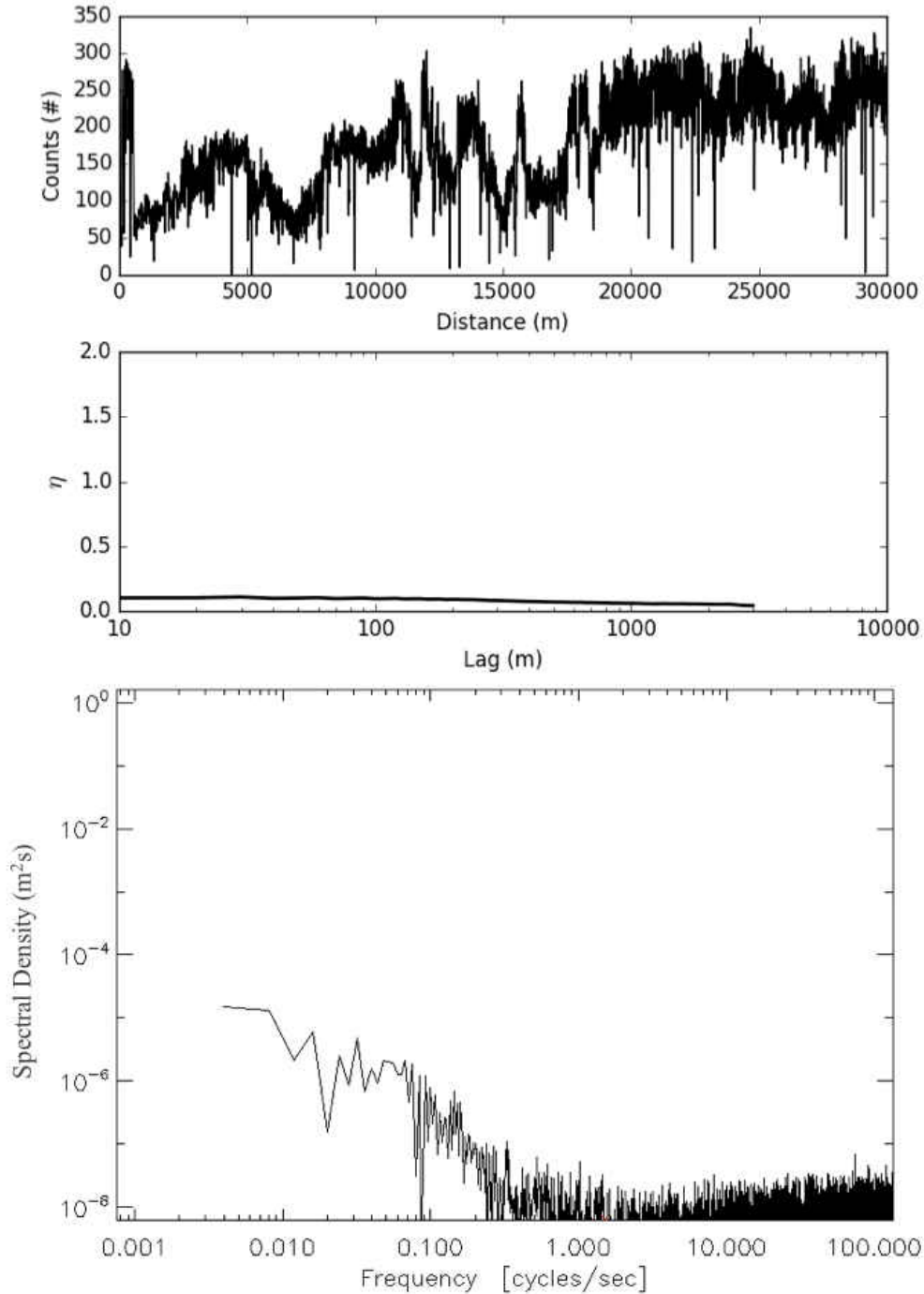


Figure 33: Counts series (top image) for the 13 Dec 2015 flight during 17:13:20 UTC-17:17:31 UTC. Data represents the number of counts observed per 10 meters. Pair correlation (middle image) derived using the counts series above. Maximum lag is one-tenth of the total flight leg distance. Spectral density (bottom image) of the derived spatial series during 17:13:20 UTC-17:17:31 UTC.

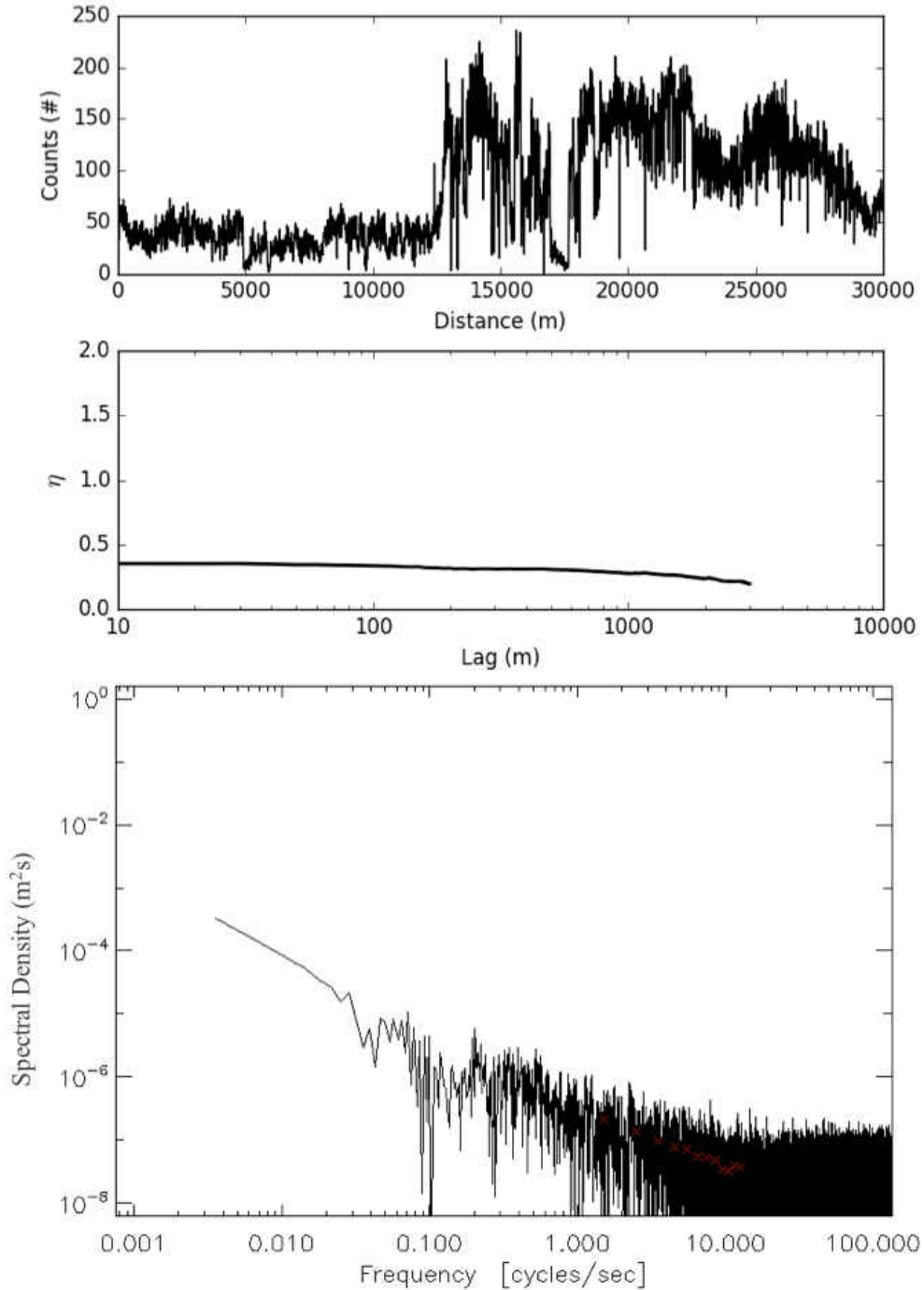


Figure 34: Counts series (top image) for the 13 Dec 2015 flight during 18:18:20 UTC-18:23:00 UTC. Data represents the number of counts observed per 10 meters. Pair correlation (middle image) derived using the counts series above. Maximum lag is one-tenth of the total flight leg distance. Spectral density (bottom image) of the derived spatial series during 18:18:20 UTC-18:23:00 UTC.

Table 7: Postfrontal flight leg averages (excluding max pair correlation). Highlighted times indicate flight legs chosen for a more thorough analysis.

Pressure Altitude	Temperature	Counts	Turbulence	Mean Volume Diameter	Mean Diameter	Max Pair Correlation
m	°C	#	$m^{2/3}s^{-1}$	μm	μm	#
4 Dec 2015						
13:32:08-13:36:22 UTC	-12	63.3	0.086	5726	1663	0.60
14:37:34-14:41:48 UTC	-3	52.3	0.087	2857	1148	0.85
14:54:34-14:58:21 UTC	-2	85.7	0.101	3819	1130	0.37
15:08:54-15:12:35 UTC	-12	101.4	0.108	8571	2283	0.48
13 Dec 2015						
16:10:00-16:14:30 UTC	-13	111.1	0.054	4635	1682	0.64
16:55:00-16:59:58 UTC	-4	106.5	0.097	4920	1411	0.26
17:04:10-17:08:45 UTC	-10	79.3	0.081	5196	1376	0.30
17:13:20-17:17:31 UTC	-15	178.8	0.043	5459	1293	0.11
17:26:40-17:30:39 UTC	-22	110.3	0.022	3586	873	0.10
18:18:20-18:23:00 UTC	-10	82.9	0.084	3496	934	0.35
18:28:20-18:32:18 UTC	-15	127.7	0.047	6298	897	0.20

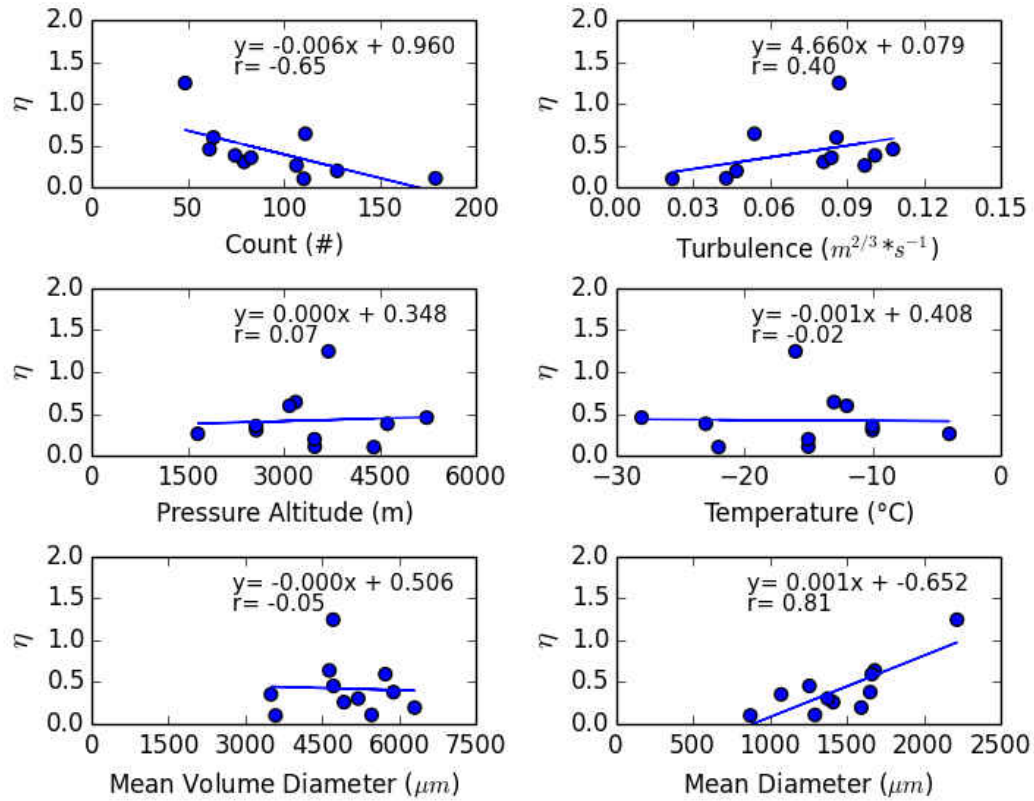


Figure 35: Postfrontal flight leg parameter averages compared to the max pair correlation. Each plot includes a linear best fit equation and correlation coefficient, r .

Discussion

Synoptic Regimes

Table 8 shows the correlation coefficient values, r , observed from each sector in regards to the relationship between the max pair correlation and derived parameters/ parameters observed in-situ. White cells indicate weak correlations (i.e. $r < 0.4$), whereas light red (light blue) cells indicate moderate positive (negative) correlations (i.e. $0.4 \leq r \leq 0.6$ ($-0.4 \geq r \geq -0.6$)). Conversely, dark red (dark blue) cells indicate strong positive (negative) correlations (i.e. $0.6 \leq r < 1.0$ ($-0.6 \geq r > -1.0$)).

Table 8: Correlation coefficient, r , from each sector in regards to the relationship between the max pair correlation and the pressure altitude, temperature (temp), counts, turbulence (turb), mean volume diameter, and mean diameter. Dark (light) red corresponds to a strong (moderate) positive correlation, and dark (light) blue corresponds to a strong (moderate) negative correlation.

		Pressure Altitude	Temp.	Counts	Turb.	Mean Volume Diameter	Mean Diameter
Prefrontal (rain)	r	0.43	-0.57	-0.93	-0.36	-0.14	0.72
Prefrontal (ice)	r	0.14	-0.02	-0.76	-0.69	-0.90	-0.52
Frontal	r	-0.17	0.18	-0.47	0.15	0.10	0.30
Postfrontal	r	0.07	-0.02	-0.65	0.40	-0.05	0.81

One relationship that is consistent among all sectors is a negative correlation between the precipitation particle counts and max pair correlation. In other words, the max pair correlation increases as the number of counts decreases. This negative correlation is stronger for prefrontal rain and prefrontal ice flight legs than for frontal and postfrontal flight legs. With respect to the mean diameter, statistics from prefrontal rain and postfrontal flight legs indicate that positive correlations exist when compared to the max pair correlation, whereas statistics from prefrontal ice flight legs indicate that a moderate negative correlation exist. However, the correlations are weaker for the prefrontal rain and postfrontal flight legs if the outlier data point in each sector is excluded. Therefore, it is important to err on the side of caution when interpreting the correlation values since the sample size for each sector is small. In regards to the pressure altitude and temperature, statistics from prefrontal rain flight legs indicate that a moderate positive and negative correlation exist respectively when compared to the max pair correlation. However, only weak correlations between these parameters are found in the remaining sectors. Lastly, with respect to turbulence and the mean volume diameter, statistics from prefrontal ice flight legs indicate that a moderate and strong negative correlation exist respectively when compared to the max pair correlation. In comparison, a moderate positive correlation exists between the max pair correlation and turbulence in the postfrontal sector.

In addition to statistical correlations, there are also a few general differences that exist among each sector. For example, this study found that higher pair correlations (i.e. greater than 1.0) occur in the prefrontal sector. This could be due to the general structure of prefrontal rainbands, which often contain pockets of little to no precipitation. As a result, certain flight legs can experience lower counts of precipitation size particles, which can

ultimately contribute to overall higher pair correlation values. The prefrontal sector also has the highest variability in the number of counts, which ranged from around 4 to nearly 200. In comparison, the frontal sector has the lowest variability in number counts along with the lowest pair correlations, as more than half were below 0.10. It should be noted that all of the flight legs in this sector, excluding the first, are vertically stacked. The radar signature also remained fairly consistent during this time period, with reflectivity values ranging between 20-25 dBZ. Thus, consistency in number of counts and pair correlation values could be a result of nearly all flight legs being stacked along with each occurring in regions of steady stratiform precipitation on the same day. Lastly, the postfrontal sector generally experienced stronger turbulence compared to any other sector, which could be due to convection that is often embedded in postfrontal rainbands.

Along with stratification by synoptic regime, flight legs were also stratified by land versus ocean and high cloud (pressure altitude) versus low cloud (pressure altitude) to determine if any additional correlations exist. However, no substantial relationships or correlations were found when using these stratifications.

Spectral Density

In regards to the spectral density, this study found consistent results among each sector. Table 9 shows that the spectral density generally starts at higher values (i.e. greater than or equal to $10^{-2} \text{ m}^2 \text{ s}$) if the max pair correlation is high and lower values (i.e. less than or equal to $10^{-4} \text{ m}^2 \text{ s}$) if the max pair correlation is low. Additionally, the correlation coefficient (Fig. 36) indicates that a moderate positive correlation exists between the max pair correlation and max spectral density. In terms of noise in the spectrum, all sectors transition from signal to noise between 700-1000 m, which indicates that there are not

many contributions to the signal at shorter distances. Lastly, with respect to minima/maxima in spectral density, all sectors generally experience a minimum at frequencies between 0.020-0.030 s⁻¹ (~ 8-9 km), which signifies a lower degree of clustering at that frequency.

Table 9: Max pair correlation and max spectral density observed for selected flight legs.

	Time	Max Pair Correlation	Max Spectral Density
Sector	UTC	#	m²s
Prefrontal Rain	16:28:30-16:33:34	0	10 ⁻³
	17:25:30-17:31:10	0.34	10 ⁻³
Prefrontal Ice	16:28:30-16:33:34	0.05	10 ⁻⁵
	17:25:30-17:31:10	1.05	10 ⁰
Frontal	16:28:30-16:33:34	0.06	10 ⁻⁴
	17:25:30-17:31:10	0.10	10 ⁻⁴
Postfrontal	16:28:30-16:33:34	0.37	10 ⁻⁵
	17:25:30-17:31:10	0.11	10 ⁻⁵
	16:28:30-16:33:34	0.35	10 ⁻³

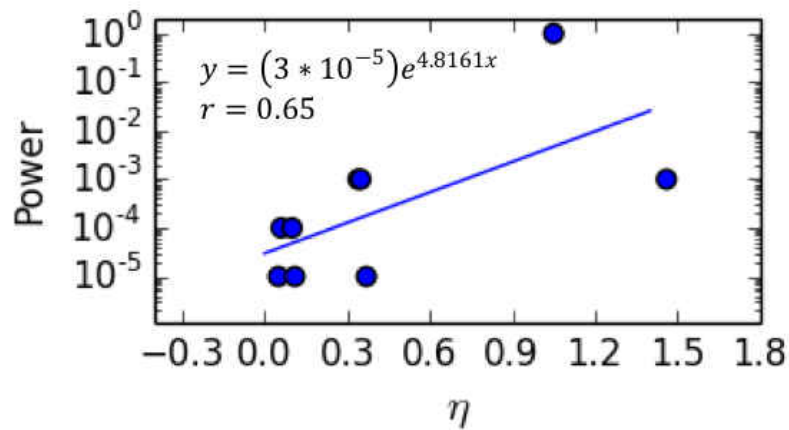


Figure 36: Max pair correlation of selected legs compared to the max spectral density. Each plot includes an exponential best fit equation and correlation coefficient, r.

CHAPTER V

CONCLUSIONS

Importance of Study

The assumption that particles follow Poissonian statistics provides the foundation for much of cloud physics. Though there is extensive knowledge concerning the clustering of cloud droplets, research concerning the clustering of precipitation size particles remains ongoing. Prior work studied the clustering of precipitation size particles using rain gauges and disdrometer networks; however, airborne observations have not been used to study such phenomena. Thus, this is the first known study to use airborne imaging probe data to examine clustering and it allows for longer spatial scales to be analyzed. This work also analyzes whether clustering changes with synoptic forcing, which has not been previously explored.

Conclusions

Using in situ observations collected during OLYMPEX, a clustering analysis is performed on multiple flight legs from each sector using the pair correlation function. Though this study has a small sample size and cannot be considered complete in any sense, results already reveal that airborne observations can be used to study the clustering of precipitation size particles and that similarities and differences do exist between synoptic regimes. The strongest finding of this study is that a negative correlation exist between the number of counts and max pair correlation. Aside from this, prefrontal rain (ice) and

postfrontal flight legs also found that a strong positive (weak negative) correlation exist between the mean diameter and max pair correlation. However, this study found no substantial correlations in terms of pressure altitude, temperature, and turbulence in relation to the max pair correlation. Therefore, the strongest finding of this study suggest that clustering is heavily tied to the structure of precipitation and the synoptic regime itself. For example, clustering is minimal in regions of steady stratiform precipitation (i.e. frontal bands), whereas, clustering is more dominant in regions of intermittent and convective precipitation (i.e. prefrontal and postfrontal bands), much like Jameson et. al (2015) found when studying clustering in stratiform and convective rain via a disdrometer network.

Implications and Future Work

One of the most important avenues of recent meteorological radar research is the application of polarization techniques to improve rainfall estimation (Jameson and Kostinski 2008). The use of differential reflectivity (Z_{DR}) provides the foundation for many of these techniques, therefore, it is important to understand the statistical accuracy of Z_{DR} . Previous work involving estimations of meteorological radar uncertainties have followed the notion that signals obey Rayleigh statistics, which assumes that all waves from each particle scatter independently and that conditions are spatially homogeneous (Jameson and Kostinski 2008). However, results from this study and previous work agree that meteorological conditions do not always satisfy the requirements for Rayleigh statistics. Using Monte Carlo simulations, Jameson and Kostinski (2008) found that the standard deviation of Z_{DR} is significantly enhanced by clustering. Thus, incorporating non-Rayleigh signal statistics into the current framework used in radar applications could provide more accuracy in terms of Z_{DR} , and other derived parameters, such as rainfall rate, which can be

heavily influenced by the presence of clustering. These improvements can also be applied to measurements from satellites such as GPM, which could help improve estimates of precipitation around mountainous regions. Nonetheless, a comprehensive view of clustering is still needed before these steps can occur. While this work has shown that clustering of precipitation size particles can be studied using airborne measurements, more clustering analyses can still be conducted on other OLYMPEX flights and on data from other field campaigns (where precipitation size airborne imaging probes are used), in order to produce a more robust data set and comprehensive view of clustering. Additionally, thresholds of clustering should be determined in order to signify what qualifies as a significant clustering signature. For example, most clustering signatures in the frontal sector were greater than zero but less than 0.1. Is this significant compared to those clustering signatures greater than 1.0 observed in the prefrontal sector? At the very least, it is time to begin to document the prevalence and magnitude of clustering and its subsequent generation of non-Rayleigh signal statistics in a wide variety of meteorological settings in order to improve quantitative applications of radar observations (Jameson and Kostinski 2008).

REFERENCES

- Baker, B. A., 1992: Turbulent entrainment and mixing in clouds: A new observational approach. *J. Atmos. Sci.*, **49**, 387-404.
- Delene, D. J., 2011: Airborne data processing and analysis software package. *Earth Science Informatics*, 4(1), 29-44.
- Delene, D. J., 2009: University of North Dakota's Citation Aircraft ASCII Data Files, Accessed 30 Jun 2018, <http://aerosol.atmos.und.edu/ADPAA/datafiles.html>.
- Field, P. R., A.J. Heymsfield, and A. Bansemmer, 2006: Shattering and Particle Interarrival Times Measured by Optical Array Probes in Ice Clouds. *J. Atmos. Oceanic Technol.*, **23**, 1357–1371.
- Hou, A. Y., R. K. Kakar, S. Neeck, A. A. Azarbarzin, C. D. Kummerow, M. Kojima, R. Oki, K. Nakamura, and T. Iguchi, 2014: The Global Precipitation Measurement Mission. *Bull. Amer. Meteor. Soc.*, **95**, 701–722.
- Houze, R. A., L. A. McMurdie, W. A. Petersen, M. R. Schwaller, W. Baccus, J. D. Lundquist, C. F. Mass, B. Nijssen, S. A. Rutledge, D. R. Hudak, S. Tanelli, G. G. Mace, M. R. Poellot, D. P. Lettenmaier, J. P. Zagrodnik, A. K. Rowe, J. C. DeHart, L. E. Madaus, and H. C. Barnes, 2017: The Olympic Mountains Experiment (OLYMPEX). *Bull. Amer. Meteor. Soc.*, **98**, 2167–2188.

- Jameson, A. R., M. L. Larsen, and A. B. Kostinski, 2015: Disdrometer Network Observations of Finescale Spatial–Temporal Clustering in Rain. *J. Atmos. Sci.*, **72**, 1648–1666.
- Jameson, A. R. and A. B. Kostinski, 2008: The Effect of Clustering on the Uncertainty of Differential Reflectivity Measurements. *J. Appl. Meteor. Climatol.*, **47**, 2816–2827.
- Knollenberg, R. G., 1970: The Optical Array: An Alternative to Scattering or Extinction for Airborne Particle Size Determination. *J. Appl. Meteor.* **9**, 86–103.
- Korolev, A. and G. A. Isaac, 2005: Shattering during Sampling by OAPs and HVPS. Part I: Snow Particles. *J. Atmos. Oceanic Technol.*, **22**, 528–542.
- Kostinski, A. B., and A. R. Jameson, 1997: Fluctuation properties of precipitation. Part I: On deviations of single-size counts from the Poisson distribution. *J. Atmos. Sci.*, **54**, 2174–2186.
- Kostinski, A. B., and R. A. Shaw, 2001: Scale-Dependent Droplet Clustering in Turbulent Clouds. *Journal of Fluid Mechanics.*, **434**, 389–398.
- Lawson, R. P., D. O’Connor, P. Zmarzly, K. Weaver, B. Baker, Q. Mo, and H. Jonsson, 2006: The 2D-S (Stereo) Probe: Design and Preliminary Tests of a New Airborne, High-Speed, High-Resolution Particle Imaging Probe. *J. Atmos. Oceanic Technol.*, **23**, 1462–1477.
- Marshak, A., Y. Knyazikhin, M. L. Larsen, and W. J. Wiscombe, 2005: Small-Scale Drop-Size Variability: Empirical Models for Drop-Size-Dependent Clustering in Clouds. *J. Atmos. Sci.*, **62**, 551–558.

- O'Brien, J., 2016: Sensitivity of Two-Dimensional Stereo (2DS) Probe Derived Parameters to Particle Orientation. M.S. thesis, Dept. of Atmospheric Sciences, The University of North Dakota, 107 pp.
- Rogers, R. R., and M. K. Yau, 1989: A Short Course in Cloud Physics. Pergamon Press, 290 pp.
- Shaw, R. A., A. B. Kostinski, and M. L. Larsen, 2002: Towards quantifying droplet clustering in clouds. *Q. J. R. Meteorolo. Soc.*, **128**, 1043-1057.
- Storelvmo, T., and I. Tan, 2015: The Wegener–Bergeron–Findeisen process—Its discovery and vital importance for weather and climate. *Meteor. Z.*, **24**, 455-461.